



RESEARCH ARTICLE

10.1029/2021GC010153

Key Points:

- Axial has re-inflated to 85%–90% of its pre-2015-eruption level but inflation has slowed and the next eruption still appears to be years away
- The rate of inflation has varied with time and the last two eruptions appear to be linked to a surge in magma supply that is now waning
- The rate of seismicity is dependent on both the level and rate of inflation consistent with a physical model of inter-eruption behavior

Supporting Information:

Supporting Information may be found in the online version of this article.

Correspondence to:

W. W. Chadwick Jr.,
william.w.chadwick@gmail.com

Citation:

Chadwick, W. W. Jr., Wilcock, W. S. D., Nooner, S. L., Beeson, J. W., Sawyer, A. M., & Lau, T.-K. (2022). Geodetic monitoring at Axial Seamount since its 2015 eruption reveals a waning magma supply and tightly linked rates of deformation and seismicity. *Geochemistry, Geophysics, Geosystems*, 23, e2021GC010153. <https://doi.org/10.1029/2021GC010153>

Received 7 SEP 2021
Accepted 17 DEC 2021

Author Contributions:

Conceptualization: William W. Chadwick, Scott L. Nooner
Data curation: William W. Chadwick, William S. D. Wilcock, T.-K. Lau
Formal analysis: William W. Chadwick, Jeffrey W. Beeson, Audra M. Sawyer
Funding acquisition: William W. Chadwick, William S. D. Wilcock, Scott L. Nooner

© 2021. The Authors.

This is an open access article under the terms of the [Creative Commons Attribution-NonCommercial-NoDerivs License](#), which permits use and distribution in any medium, provided the original work is properly cited, the use is non-commercial and no modifications or adaptations are made.

Geodetic Monitoring at Axial Seamount Since Its 2015 Eruption Reveals a Waning Magma Supply and Tightly Linked Rates of Deformation and Seismicity

William W. Chadwick Jr.¹ , William S. D. Wilcock² , Scott L. Nooner³ , Jeffrey W. Beeson^{1,4} , Audra M. Sawyer³, and T.-K. Lau¹

¹CIMRS, Hatfield Marine Science Center, Oregon State University, Newport, OR, USA, ²School of Oceanography, University of Washington, Seattle, WA, USA, ³University of North Carolina Wilmington, Wilmington, NC, USA, ⁴NOAA, Pacific Marine Environmental Laboratory, Newport, OR, USA

Abstract Axial Seamount is a basaltic hot spot volcano with a summit caldera at a depth of ~1,500 m below sea level, superimposed on the Juan de Fuca spreading ridge, giving it a robust and continuous magma supply. Axial erupted in 1998, 2011, and 2015, and is monitored by a cabled network of instruments including bottom pressure recorders and seismometers. Since its last eruption, Axial has re-inflated to 85%–90% of its pre-eruption level. During that time, we have identified eight discrete, short-term deflation events of 1–4 cm over 1–3 weeks that occurred quasi-periodically, about every 4–6 months between August 2016 and May 2019. During each short-term deflation event, the rate of earthquakes dropped abruptly to low levels, and then did not return to higher levels until reinflation had resumed and returned near its previous high. The long-term geodetic monitoring record suggests that the rate of magma supply has varied by an order of magnitude over decadal time scales. There was a surge in magma supply between 2011 and 2015, causing those two eruptions to be closely spaced in time and the supply rate has been waning since then. This waning supply has implications for eruption forecasting and the next eruption at Axial still appears to be 4–9 years away. We also show that the number of earthquakes per unit of uplift has increased exponentially with total uplift since the 2015 eruption, a pattern consistent with a mechanical model of cumulative rock damage leading to bulk failure during magma accumulation between eruptions.

Plain Language Summary Axial Seamount is an underwater volcano located offshore Oregon, USA, that is frequently active and an ideal site for studying volcanic eruptions, hydrothermal vents, and deep-sea ecosystems. Axial is monitored by a network of seafloor instruments connected to shore by a fiber-optic cable, which is part of the Ocean Observatories Initiative, supported by the National Science Foundation. Monitoring of vertical movements of the seafloor at Axial have shown that it has a repeatable pattern of inflation and deflation that can be used for eruption forecasting. Since its last eruption in 2015, Axial has re-inflated almost to the level of its previous high, but we believe the next eruption is still some years away because the rate of inflation is currently quite low. The monitoring data also show that the rates of earthquakes and uplift are evolving in a predictable way with time, because they are both related to the on-going magma accumulation, which causes the uplift, stresses the crust, and generates earthquakes. Eventually that increasing stress will open a pathway for magma, which will lead to an eruption. This work seeks to understand these processes so that we can better predict the behavior of Axial Seamount and other active volcanoes.

1. Introduction

Axial Seamount is an active submarine volcano with a summit caldera at ~1,500 m depth and a base at ~2,400 m, located about 500 km offshore Oregon, USA (Figure 1). It is a basaltic shield with a magma supply fed by the Cobb hotspot superimposed on the Juan de Fuca spreading ridge (Chadwick et al., 2005; Embley et al., 1990). It has erupted 3 times in the last 23 years: in 1998, 2011, and 2015 (Caress et al., 2012; Chadwick et al., 2013, 2016; Clague et al., 2017, 2018; Embley et al., 1999) and is currently building to its next eruption. It has by far the longest record of geodetic monitoring of any submarine volcano, dating back to the early 1980s (Chadwick et al., 2012; Chadwick, Nooner, et al., 2006; Fox, 1990, 1993, 1999; Nooner & Chadwick, 2009, 2016). This monitoring has been accomplished with various kinds of bottom pressure recorders (BPRs; also known as absolute pressure gauges, or APGs) that can be used as a proxy for depth to monitor vertical movements of the seafloor.

Investigation: William W. Chadwick, William S. D. Wilcock, Scott L. Nooner, Jeffrey W. Beeson, Audra M. Sawyer

Methodology: William W. Chadwick, William S. D. Wilcock, Scott L. Nooner, Audra M. Sawyer

Project Administration: William W. Chadwick, William S. D. Wilcock, Scott L. Nooner

Software: William W. Chadwick, William S. D. Wilcock, Audra M. Sawyer, T.-K. Lau

Validation: T.-K. Lau

Visualization: William W. Chadwick, William S. D. Wilcock, Jeffrey W. Beeson

Writing – original draft: William W. Chadwick

Writing – review & editing: William S. D. Wilcock, Scott L. Nooner, Jeffrey W. Beeson

The early years of monitoring at Axial were performed by autonomous, battery-powered BPR instruments that were repeatedly deployed for 1–3 years at a time and then recovered. Since 2000, campaign-style measurements have also been made every few years with a Mobile Pressure Recorder (MPR) at an array of seafloor benchmarks with a remotely operated vehicle (ROV) (Chadwick et al., 2012; Chadwick, Nooner, et al., 2006; Nooner & Chadwick, 2009). Then in late 2014, the Ocean Observatories Initiative's (OOI) Regional Cabled Array (RCA) came on-line, which provides power and bandwidth to a network of seafloor monitoring instruments at Axial Seamount via a fiber-optic cable connected to shore, including four BPR/tilt instruments and seven seismometers (Kelley et al., 2014). This enables continuous long-term monitoring with real-time data from a diverse set of instrumentation. For example, the cabled observatory was in place during the April 2015 eruption, providing an extraordinary inter-disciplinary data set that has been used to interpret that event in rich detail (Baillard et al., 2019; Caplan-Auerbach et al., 2017; Clague et al., 2017, 2018; Hefner et al., 2020; Le Saout et al., 2020; Levy et al., 2018; Nooner & Chadwick, 2016; Waldhauser et al., 2020; Wilcock et al., 2016; Xu et al., 2018). Other data sets that provide valuable information on the crustal structure and magma storage system beneath Axial Seamount were collected by a seismic tomography study (West et al., 2001) and two multi-channel seismic reflection surveys, one 2-D survey performed in 2002 (Arnulf et al., 2014, 2018) and a 3-D survey in 2019 (Arnulf et al., 2019, 2020), which have revealed the location and geometry of a large shallow magma reservoir 1.5–2.5 km below the caldera, and a series of deeper stacked sills from 2.5 to 4.5 km depth below the southern caldera (Carbotte et al., 2020).

The geodetic monitoring has shown that the pattern of co-eruption deflation and inter-eruption re-inflation at Axial Seamount appears to be fairly repeatable, which was used to successfully forecast the 2015 eruption within a 1-year time window, 7 months in advance (Cabaniss et al., 2020; Nooner & Chadwick, 2016). Today, continuous geodetic monitoring at Axial uses a combination of the four OOI-BPR/tilt instruments, four uncabled autonomous BPR moorings, and eight additional mini-BPRs that are deployed and recovered by an ROV on the MPR benchmarks, in addition to the campaign-style MPR measurements every 2 years. In addition, repeated bathymetric surveys by autonomous underwater vehicles (AUVs) have been used since 2011 to detect depth changes at lower resolution but over a larger area (Caress et al., 2015, 2016, 2020; Hefner et al., 2021; Nooner et al., 2017).

Here, we present BPR time-series data during the re-inflation of the volcano since its 2015 eruption, focusing mainly on its temporal evolution and its relation to seismicity. The BPR data show a slowing rate of inflation with time, and superimposed on that we identify eight repeated short-term deflation events between 2016 and 2019 that were co-incident with a sharp reduction in the rate of seismicity (Natalie et al., 2018). The decrease in inflation rate reflects changes in the magma supply to the volcano, which in turn have implications for eruption forecasting. Finally, we show that the deformation and seismicity are tightly linked and are evolving with time as predicted by a physical model of the changing proportion of elastic and inelastic deformation during inter-eruption magma accumulation.

2. Methods

The continuously recording BPRs that we have used at Axial Seamount use pressure sensors made by Paroscientific, Inc., and record every 15 or 100 s in the uncabled instruments, and at a rate of 20 Hz in the cabled instruments. For seafloor geodesy, the pressure data are first converted to equivalent depth and are de-tided. To remove the tides, we subtract a predicted tide model (Pawlowicz et al., 2002), which retains high-frequency information in the records that may be of interest. The remaining signal has several non-geophysical sources of noise that have to be accounted for: instrumental drift (up to ~20 cm/yr) (Polster et al., 2009), tidal residuals of ± 5 cm at tidal frequencies, and non-tidal oceanographic signals (due to winds, atmospheric pressure changes, ocean circulation, etc.) of ± 5 cm at periods of days to weeks (Dobashi & Inazu, 2021; Inazu et al., 2012).

Drift is not a significant problem for detecting short-term events (over days to weeks), such as co-eruption deflation, but it is a major concern for measuring long-term inflation, because drift can be of the same magnitude. To address the drift issue, we have used the ROV-based MPR measurements to make surveys at an array of 10 seafloor benchmarks every 1–3 years, by using one benchmark located 10 km south of the center of the caldera as a reference site (AX-105 in Figure 1, assumed to be stable) and computing the relative depths of the other benchmarks in or near the caldera with a repeatability of ± 1 cm (Chadwick et al., 2012; Chadwick, Nooner, et al., 2006; Nooner & Chadwick, 2009, 2016). The MPR measurements can also constrain the drift of any BPRs that are co-located at the benchmarks. For example, the MPR data from 2015 to 2020 have shown that the OOI

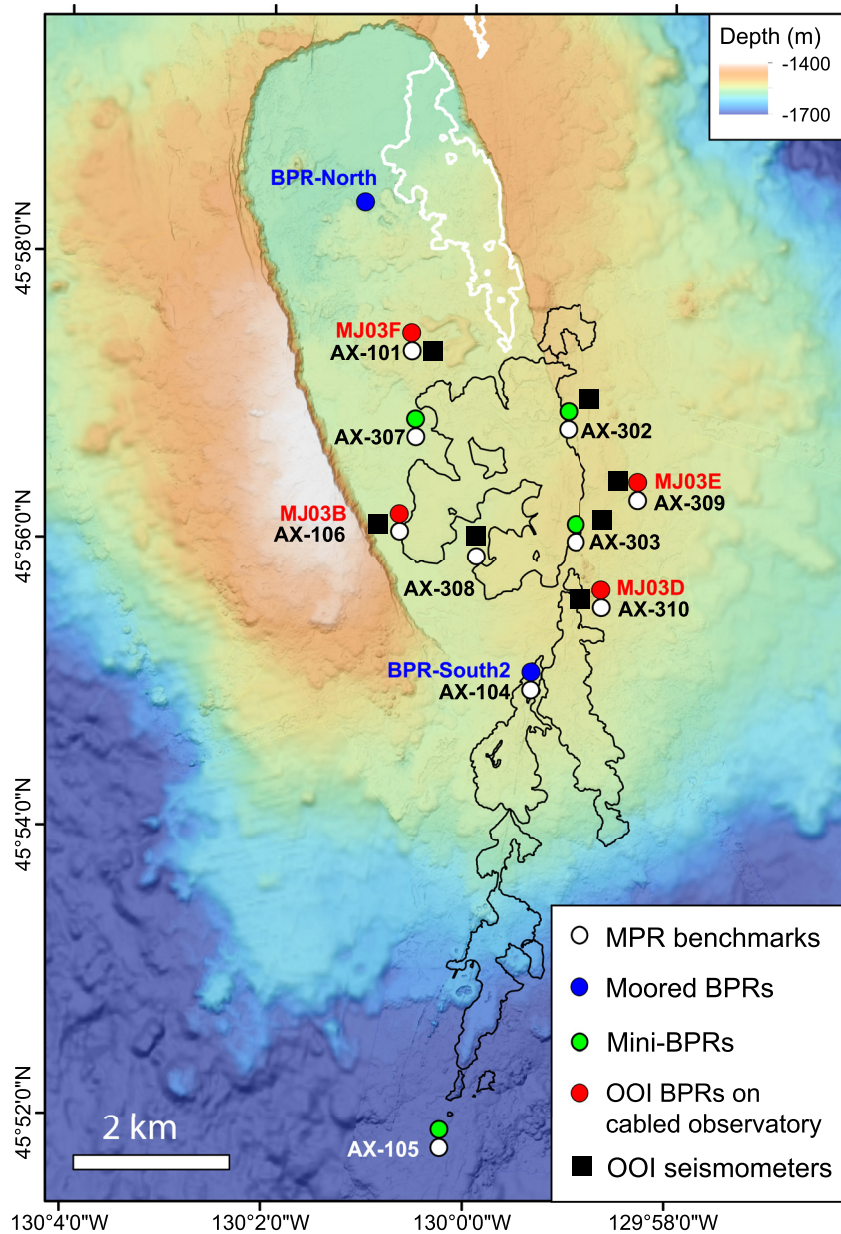


Figure 1. Bathymetric map of the summit caldera of Axial Seamount showing network of bottom pressure recorders (BPRs) that were on the seafloor in June 2018 (colored dots). Red dots are BPRs connected to the OOI Cabled Observatory, blue dots are moored-BPRs, and green dots are mini-BPRs deployed on seafloor benchmarks (white dots) where campaign-style MPR measurements are made. *Differential* BPR records are created by subtracting OOI-BPR MJ03E (Eastern Caldera) from MJ03F (Central Caldera), or by subtracting the mini-BPR record at benchmark AX-105 (the MPR reference station) from the others. Black and white outlines are lava flows erupted in 2011 and 2015, respectively. Black squares are OOI seismometers.

BPRs all have negligible drift rates (<0.5 cm/yr). All the BPR data presented in this paper are either drift-corrected or did not need correcting. Other more recent approaches to quantifying BPR drift use modified sensors with a known reference pressure to compare with the ambient pressure over time (Cook et al., 2019; Manalang et al., 2019; Sasagawa & Zumberge, 2021; Sasagawa et al., 2016; Wilcock et al., 2021), some of which are being tested at Axial, but we do not employ these methods here. However, these self-calibrating BPRs could be used as a reference site for MPR measurements in the future.

The de-tided and drift-corrected BPR data are still overprinted with tidal residuals and non-tidal oceanographic noise. In other settings, two approaches have been used to remove the latter by either subtracting pressure

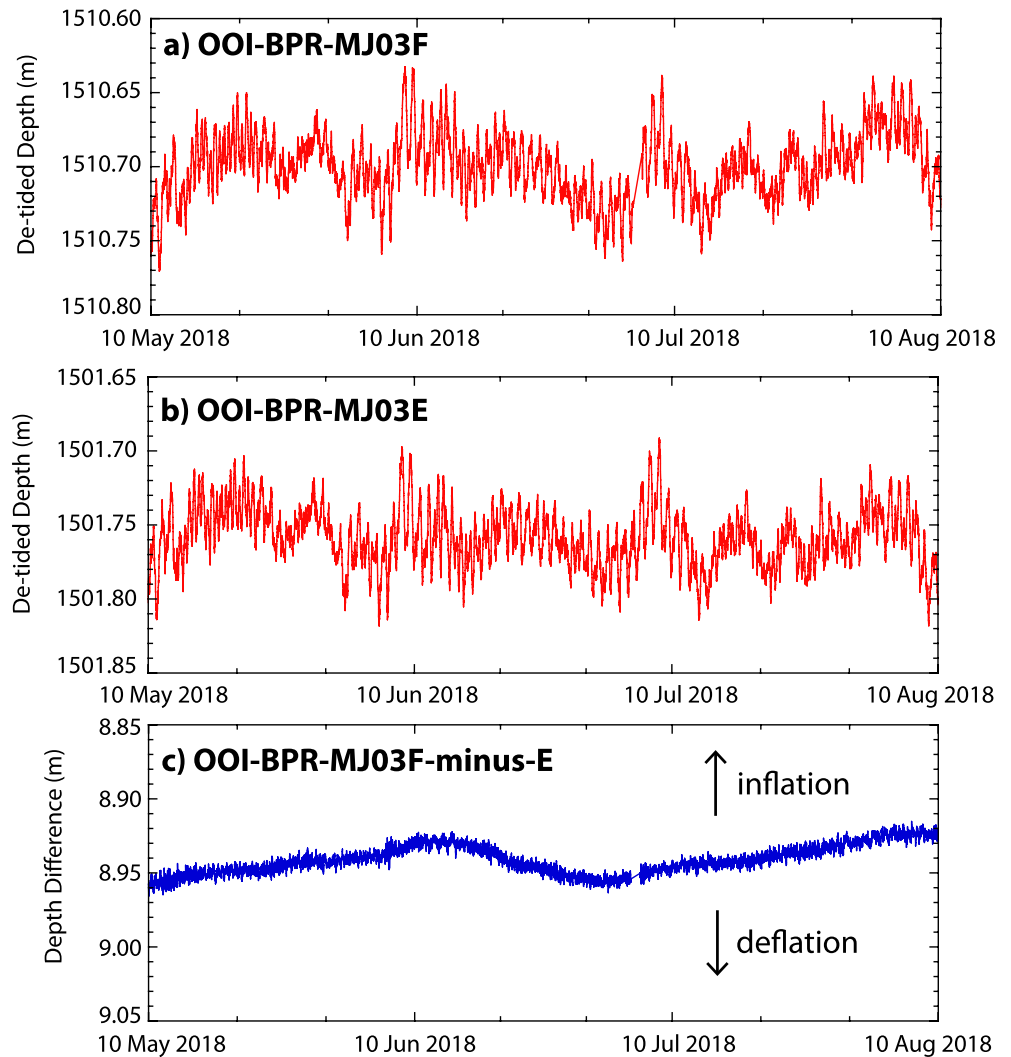


Figure 2. Comparison of de-tided *single-station* bottom pressure recorder (BPR) data with *differential* BPR data. (a) Three months of de-tided data from OOI-BPR-MJ03F at the Central Caldera, overprinted with higher-frequency tidal residuals and lower-frequency non-tidal oceanographic noise. (b) De-tided data from OOI-BPR-MJ03E at the Eastern Caldera over the same time period, showing a similar pattern of noise. (c) *Differential* BPR record over the same time period, created by subtracting (b) from (a), which removes the common sources of noise and makes the geodetic signal much clearer. All three plots have the same scale on the y-axis (20 cm). The OOI-BPRs at MJ03F and MJ03E consistently have the largest and smallest vertical movements, respectively, so their differential record best isolates the geodetic signal. Locations of BPRs are shown in Figure 1.

variation predicted by a global ocean model (Dobashi & Inazu, 2021; Inazu et al., 2012; Muramoto et al., 2019) or by subtracting the record of a nearby BPR that is outside the zone of deformation but experiences nearly the same oceanographic noise (Fredrickson et al., 2019; Wallace et al., 2016). For the BPR data from Axial, we have chosen to subtract data from a reference BPR in one of two ways. For the OOI cabled BPR data, we subtract data from the BPR with the smallest deformation signal (MJ03E) located on the east rim of the caldera, from the BPR with the largest deformation signal (MJ03F) located at the center of the caldera (Figures 1 and 2). For non-cabled BPR data recorded on the MPR benchmarks, we use data from benchmark AX-105 (farthest from the caldera) as a reference (Figure 1). In either case, this has the desired effect of removing most of the tidal and non-tidal oceanographic signals that are common to both instruments, since they are located at similar depths only a few km apart. This reduces the noise level from ± 5 to ± 1 cm and yields a *differential* BPR record that is a much clearer representation of the geophysical signal in which we are interested (Figure 2). Throughout the rest of this paper, we will differentiate between *differential* BPR data, and data from a *single-station* BPR. Both are valuable since

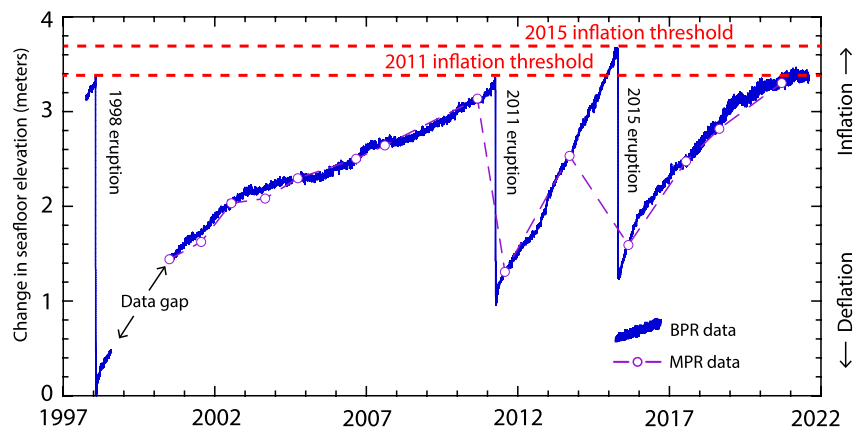


Figure 3. Long-term *single-station* bottom pressure recorder (BPR) record from the Central Caldera (near MJ03F and AX-101 in Figure 1) showing vertical movements of the seafloor over time. The blue curve is BPR data from multiple non-cabled instruments before 2017 and from OOI-BPR MJ03F since 2017. Purple dots are MPR data used to tie multiple records together and to remove drift from the BPR data. Note that the relative displacement across the data gap between 1998 and 2000 is unknown. Plot shows the major short-term deflation during eruptions in 1998, 2011, and 2015 and long-term re-inflation between eruptions at variable rates. The overall deformation cycle appears to be inflation-predictable, which can be used to forecast eruptions.

the *single-station* BPR data provide information on seafloor deformation at specific sites, how it varies spatially, and can be modeled or used to calculate magma supply rates, whereas the *differential* BPR data provide a clearer view of temporal trends and changes in uplift rates. Experience has shown that the MJ03F-MJ03E *differential* BPR uplift (the caldera center relative to the eastern caldera reference) is about 60% of the *single-station* uplift measured at the caldera center BPR. Therefore multiplying the MJ03F-MJ03E *differential* BPR data by 1.67 approximates the true uplift at the caldera center (and without most of the oceanographic noise). Near-real-time data from *single-station* OOI BPRs, and the MJ03F-MJ03E *differential* BPR time-series, are displayed at this web site: <https://www.pmel.noaa.gov/eoi/rsn/>.

Below, we compare the BPR data since the 2015 eruption to the temporal and spatial variations of earthquakes at Axial Seamount to gain insight into the magma supply and storage system. The seismic data from the OOI seismometers are processed automatically to yield histograms of the number of “volcano-tectonic” (VT) earthquakes with time and maps of their epicenters (Wilcock et al., 2016, 2017, 2018). A near-real-time catalog of the earthquake detections at Axial Seamount is available at this web site: <http://axial.ocean.washington.edu/>.

3. Results

Figure 3 is a long-term plot of the *single-station* BPR record of inflation and deflation at the center of Axial caldera. The plot shows co-eruption deflation of 2.5–3.2 m during the three eruptions, and inter-eruption re-inflation at a rate that has varied significantly with time (10–100 cm/yr). It also shows that the deformation cycle is fairly repeatable, in that eruptions appear to be triggered at a similar inflation threshold, but it is not exact. For example, the inflation threshold reached before the 2015 eruption was 30 cm higher than the one reached in 2011. Also, the exact relationship between the 1998 and 2011 inflation thresholds is unknown because of the data gap between 1998 and 2000, but nevertheless this pattern can be used as an empirical basis for forecasting the timing of future eruptions based simply on pattern recognition (Nooner & Chadwick, 2016). Physics-based modeling in hindsight suggests that the repeatable pattern may be due to a critical threshold of internal pressure required to cause magma reservoir failure (Cabaniss et al., 2020).

We know from previous studies of the seismicity at Axial that the number of earthquakes is very low immediately after an eruption for months to years, and it gradually increases with time leading up to the next eruption (Dziak & Fox, 1999; Dziak et al., 2012; Sohn et al., 1999, 2004; Wilcock et al., 2016, 2018). For example, the peak earthquake rate increased from several hundred to several thousand per day during the final 4 months before the 2015 eruption, but then dropped to only a few tens per day after the eruption (Wilcock et al., 2016). Most earthquakes at Axial are between magnitudes 0–2 (the magnitude of completeness is ~ 0), and their mean moments do

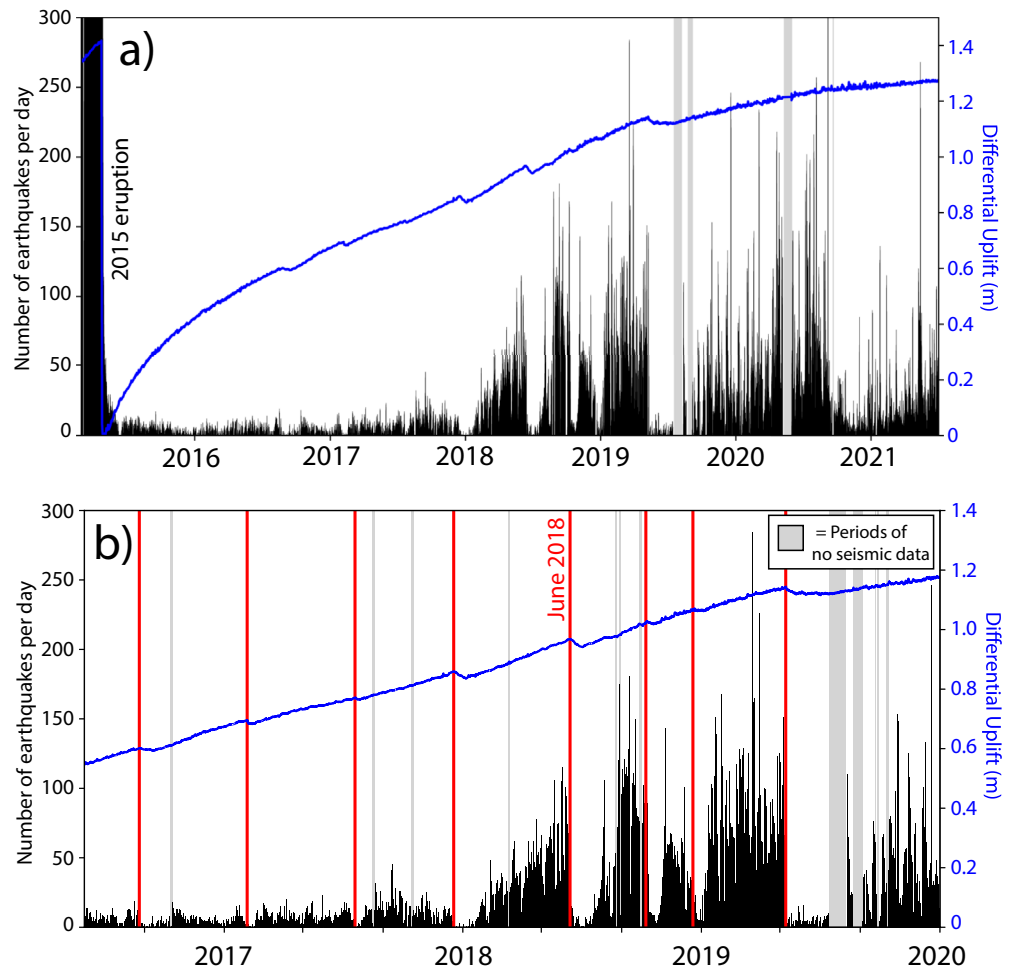


Figure 4. Plots of *differential* OOI-BPR data (blue curves) over histograms of the number of earthquakes per day (black bars) showing how deformation and seismicity have co-varied. (a) All data since the 2015 eruption. (b) Data between mid-2016 to 2020, with the start times of the eight identified short-term deflation events shown by vertical red lines (June 2018 event, shown in more detail in Figure 5, is labeled). Gray vertical stripes show times when no seismic data are available from the Wilcock et al. (2017) catalog (including 3-week period of a multi-channel seismic survey in August 2019). Differential BPR data are uncorrected.

not change significantly with time between eruptions (Tan et al., 2019; Wilcock et al., 2016, 2017), so we focus here on earthquake counts versus time. Most detected earthquakes occur within outwardly dipping fault zones beneath the eastern and western sides of the caldera at depths of <2 km between the shallow magma reservoir and the surface (Waldhauser et al., 2020; Wilcock et al., 2016, 2018). Remarkably, the same faults appear to slip, but in different directions, during inflation (normal slip) and deflation (reverse slip) (Levy et al., 2018). A few earthquakes also occur on the inwardly dipping faults that define the caldera rim at the surface (Arnulf et al., 2018; Baillard et al., 2019; Waldhauser et al., 2020), but these faults are largely aseismic presumably due to their shallow depth. The overall geometry of the inwardly and outwardly dipping faults resembles orientations found in analog experiments of caldera collapse (Acocella, 2007; Roche et al., 2000).

Figure 4a compares the record of re-inflation to the seismicity observed since the 2015 eruption. The plot shows that the seismicity at Axial remained at a very low level (~10 per day) for several years, despite a relatively high rate of re-inflation right after the eruption (>100 cm/yr). Then in 2017 or early 2018, the rate of seismicity began to gradually increase, after the volcano had recovered ~60% of the subsidence that occurred during the 2015 eruption. The rate of seismicity rose to peaks of a few hundred events per day by mid-2019, but has been quite variable since then (Figure 4a).

Table 1
Axial Seamount Short-Term Deflation Events Identified Since the 2015 Eruption

Short-term deflation event ID	Start of deflation event	End of deflation event	Date reinflated to previous level	Differential-BPR deflation amplitude (cm)	Deflation duration (days)
August 2016	24 August 2016	14 September 2016	28 September 2016	1.0	21
February 2017	5 February 2017	12 February 2017	1 March 2017	1.2	7
July 2017	20 July 2017	25 July 2017	2 August 2017	0.7	5
December 2017	18 December 2017	5 January 2018	4 February 2018	2.3	18
June 2018	14 June 2018	2 July 2018	1 August 2018	2.7	18
October 2018	8 October 2018	20 October 2018	31 October 2018	0.7	12
December 2018	19 December 2018	4 January 2019	11 January 2019	0.7	26
May 2019	10 May 2019	26 May 2019 ^a	5 September 2019	2.4	16

^aReinflation after the May 2019 deflation event didn't start until 22 July 2019, ~2 months after deflation stopped.

We have identified eight “short-term deflation events” in the differential re-inflation data, characterized by 1–4 cm of deflation over 1–3 weeks (Figure 4b and Table 1). These occurred from mid-2016 to mid-2019 and appeared to be quasi-periodic, occurring about every 4–6 months. During each short-term deflation event, the level of seismicity dropped to low levels for about a month. The close linkage between the rates of deformation and seismicity is most obvious in the later deflation events when overall seismicity rates were higher. Figure 5a shows differential BPR data over 3 months during the June 2018 deflation event (2.7 cm over 18 days), and Figure 5b is a histogram of earthquakes per day over the same time period, showing that the number of earthquakes dropped to low levels during the deflation event and did not return to higher levels until the volcano had re-inflated near the level it was at when the deflation event began. All the other short-term deflation events display a similar pattern (see Supporting Information S1), except the last one in May 2019. Figures 5c and 5d show differential BPR data and a histogram of seismicity for that event (2.4 cm of deflation over 16 days), which was different in that it was followed by 2 months of no inflation in the differential BPR record while the level of seismicity remained low. When re-inflation resumed it was at a distinctly slower rate than before the event.

4. Discussion

4.1. Possible Causes of the Short-Term Deflation Events

We consider two possible mechanisms to explain the short-term deflation events. The multichannel-seismic reflection data show that the magma storage system at Axial Seamount consists of a shallow magma reservoir about 1.5–2.5 km beneath the seafloor, underlain by a series of stacked sills that apparently feed magma upward (Arnulf et al., 2014, 2018; Carbotte et al., 2020). Specifically, Carbotte et al. (2020) infer that melt ascends through the stacked sills by porous flow and that the melt-rich layers form by mush compaction in a viscoelastic matrix. Building on the conceptual model developed by Nooner and Chadwick (2009), Figure 6a depicts an interpretive cross-section in which inter-eruption inflation is occurring as magma is supplied upward through the sill complex to the shallow magma reservoir. This increases the pressure in the shallow reservoir, which causes inflation, increases the stress in the overlying crust, and generates earthquakes on the caldera-related faults.

One hypothesis for the short-term deflation events is that they could be caused by magma moving laterally out of the shallow magma reservoir beneath the caldera, either into one of the rift zones or perhaps into a satellite reservoir (Figure 6b) such as the one imaged seismically ~8 km to the east of the caldera (Arnulf et al., 2014, 2018). This would reduce the pressure in the main reservoir, cause deflation, and effectively turn off the earthquakes in the caldera. If this were happening we might see some evidence of where the magma was moving, such as inflation occurring somewhere outside the caldera or possibly earthquakes along the magma path or surrounding the satellite reservoir (Figure 6b).

Expanding on the work of Sawyer et al. (2019) and Sawyer (2020), we examine data recorded by nine cabled and non-cabled BPR instruments throughout the caldera during the June 2018 short-term deflation event, using a 10th

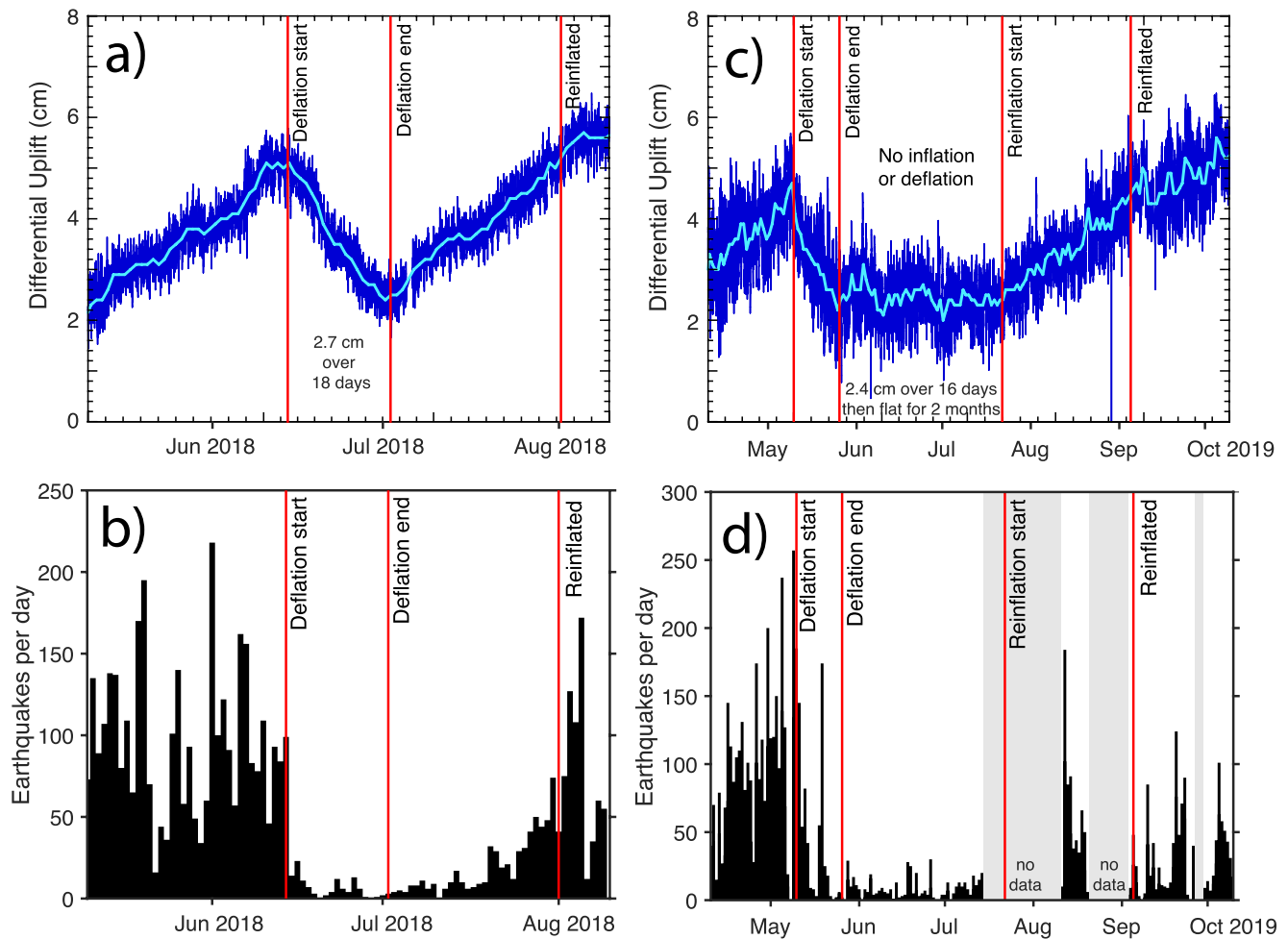


Figure 5. Deformation and seismic data during the June 2018 and May 2019 short-term deflation events. (a) Uncorrected differential bottom pressure recorder (BPR) data over 3 months from 10 May to 10 August 2018. Dark-blue curve is data sub-sampled to every 15 min; light-blue curve is data averaged over 1-day windows. Vertical red lines show the times when deflation started, ended, and when re-inflation reached the previous level. (b) Histogram of the number of earthquakes per day over the same time interval as in (a). Comparing the two plots shows that the seismicity sharply decreased during the short-term deflation event and did not increase again until re-inflation neared the previous level. (c) Uncorrected differential BPR data over 6 months from 10 April to 10 October in 2019. (d) Histogram of earthquakes during same time period as in (c). Gray bars show periods when seismic data are unavailable. Note period of 2 months following the end of the May 2019 deflation event with no inflation or deflation when seismicity remained low. Similar records for the other short-term deflation events are provided in Supporting Information S1.

BPR record from the southern-most MPR benchmark (AX-105) as a reference to create *differential* BPR records that better isolate the geodetic signal (Figure 7a). These data show that all the BPRs recorded subsidence during the short-term deflation event, confirming that its spatial extent covered the entire caldera (Figures 1 and 7b). Modeling the subsidence following Sawyer et al. (2019) and Sawyer (2020), gives a best-fit solution (Figures 7b and 7c) similar to the deformation model of Nooner and Chadwick (2016), a steeply dipping prolate spheroid located near the eastern rim of the caldera (the latter based on the much larger co-eruption deflation measured between 2013 and 2015). This shows that the deformation source during the June 2018 short-term deflation event was similar to that observed at other times (during both inflation and deflation), suggesting that the deflation events are not due to local redistribution of magma within the subcaldera reservoir. There is no evidence for inflation occurring outside the caldera during the short-term deflation events, although we have few observations there and none over the eastern satellite body.

The spatial pattern of seismicity does not change markedly during the short-term deflation events. Figure 8a is a map of earthquake epicenters from the catalog of Wilcock et al. (2017) during the 3 weeks before the June 2018 deflation event, and Figure 8b is a similar map during the following 3-weeks of deflation. Comparing the

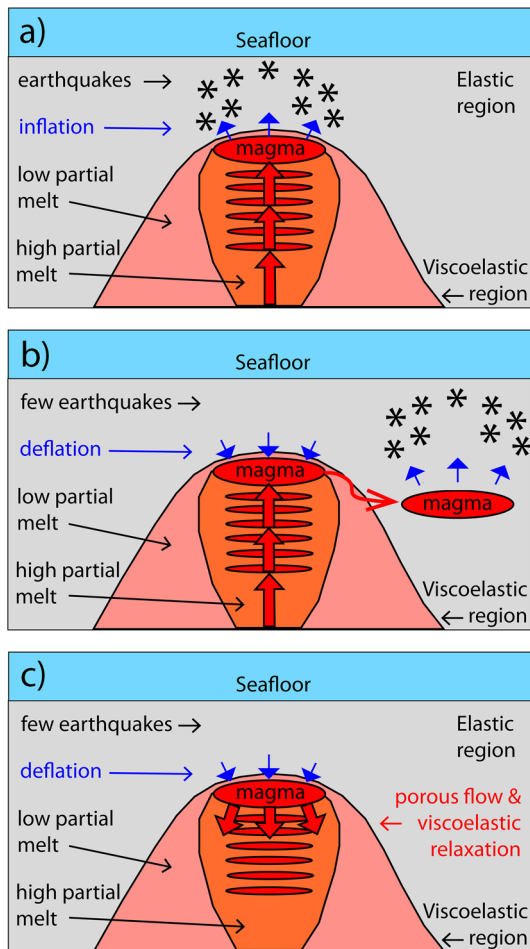


Figure 6. Cartoon illustrating two possible hypotheses to explain the short-term deflation events at Axial Seamount. (a) Idealized cross-section showing shallow magma reservoir and underlying stacked sills within a viscoelastic region of partial melt (modified from Nooner and Chadwick [2009], and based on results from Arnulf et al. [2018] and Carbotte et al. [2020]). During re-inflation, magma is supplied upward through the stacked sills to the shallow reservoir, where increasing pressure causes uplift (elastic deformation) and earthquakes (inelastic deformation) in the overlying crust. (b) One hypothesis for the short-term deflation events is that magma is transferred laterally to a satellite reservoir, which would cause deflation and a reduction in seismicity in the caldera, but might be expected to cause uplift and increased seismicity elsewhere. (c) An alternative hypothesis is that the deep supply of magma is temporarily interrupted and the deflation is due to viscoelastic relaxation and porous flow out of the shallow magma reservoir into its surroundings. See text for discussion.

two shows that the seismicity is in essentially the same pattern, but there are just fewer earthquakes during the deflation event. Similarly, Figure 8c shows the earthquakes during the following month after the deflation event had ended and the volcano was re-inflating, and Figure 8d shows the pattern of earthquakes after the volcano had re-inflated beyond the previous level and a higher level of seismicity had resumed. Again, the spatial distribution of earthquakes is similar during the two time periods. The pattern of seismicity during the other short-term deflation events is similar (see Supporting Information S1). These observations do not support or refute the hypothesis of lateral magma movement out of the subcaldera reservoir, but require that it occurs aseismically if it is happening.

An alternative hypothesis is that the supply of magma to the shallow reservoir is temporarily interrupted during these short-term deflation events (Figure 6c). During the time that the supply stops, the viscoelastic region surrounding the reservoir relaxes, outwardly directed porous flow from the shallow reservoir reduces its internal pressure, which leads to deflation and a drop in the stresses driving the seismicity. This idea perhaps seems more likely during a period when the rate of inflation (and magma supply) are decreasing, whereas the first hypothesis might be more likely during a period of increasing inflation and magma supply rate. However, the observed rate of subsidence during the short-term deflation events (~ 50 cm/yr) seems higher than one might expect for a viscoelastic relaxation mechanism, and it does not appear to decrease exponentially which also might be expected. Therefore, we do not have enough clear evidence to favor one hypothesis over the other, and conclude that more observational data and perhaps viscoelastic modeling is needed to resolve this question. Similar short-term deflation events were observed at Kilauea volcano, Hawaii, between at least 2000–2013 and were interpreted as pressure transients in a shallow magma reservoir (K. R. Anderson et al., 2015), but their underlying cause is ambiguous (A. N. Anderson et al., 2020).

4.2. The May 2019 Short-Term Deflation Event and Changes in Inflation Rate

Compared with previous short-term deflation events, the May 2019 episode was different in that it was followed by 2 months of no inflation while the seismicity remained low (Figures 5c and 5d). This time period without inflation or deflation could be interpreted as either a period of no magma supply, or a period when the magma supply had resumed but at such a low rate that it approximately counterbalanced the rate of viscoelastic relaxation or porous flow out of the magma reservoir into the surrounding crystal mush (Figure 6). In any case, the May 2019 event also marked a distinct decrease in the long-term rate of inflation. This is shown in Figure 9 in which the average rate of corrected differential uplift is calculated for each interval between the eight short-term deflation events, and also for two (somewhat arbitrary) time

periods before and after them. A case can be made that the average rate of uplift also changed to a lesser extent between some of the other short-term deflation events. Another major decrease in uplift rate occurred around August to September 2020 when there was no obvious deflation event but there was a distinct decrease in the rate of seismicity (Figure 4a).

Figure 9 shows that right after the 2015 eruption, the rate of re-inflation was relatively high, an average of 103 cm/yr between May 2015 and January 2016, but was already decreasing. The rate continued to decrease between January 2016 and May 2019, when the average rate was between 35 and 55 cm/yr. Then after May 2019,

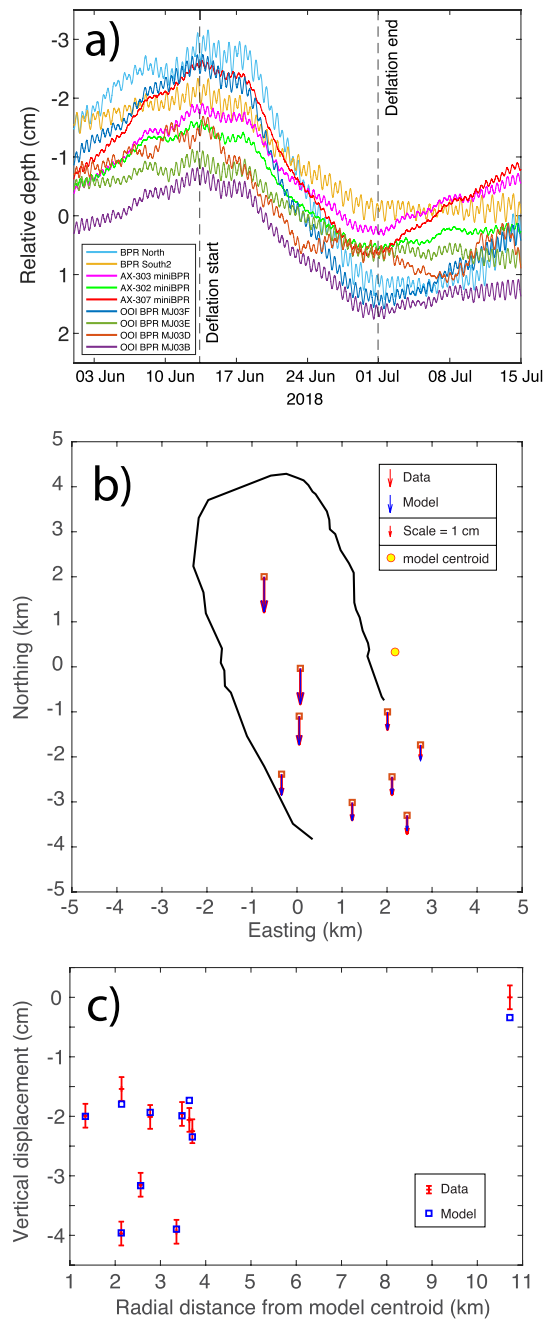


Figure 7. Differential bottom pressure recorder (BPR) records from nine sites during the June 2018 short-term deflation event, created using the data from the mini-BPR at benchmark AX-105 as a reference (see Figure 1 for locations). (a) Each BPR record has had a mean depth subtracted so they can be plotted together. Arbitrary offsets were added to aid visibility and the data smoothed with a running average. The vertical dashed lines show the start and end of the short-term deflation event in the records. (b) Comparison of vertical displacements from the best-fit deformation model (in blue) with data (in red) in map view (black line is caldera outline; yellow dot is model centroid). (c) Comparison of best-fit model (in blue) and data (in red) in plot of vertical displacement versus radial distance from the model centroid. Best-fit prolate spheroid deformation model (Battaglia et al., 2013; Yang et al., 1988) for this event has a major axis dipping at 74° in the direction of 338° , with major and minor axes of 650 and 46 m, respectively, and a depth to center of 3.7 km, similar to the best-fit source of Nooner and Chadwick (2016). The model reduced chi-square is 1.7 and the standard deviation of residuals is 1.82 mm.

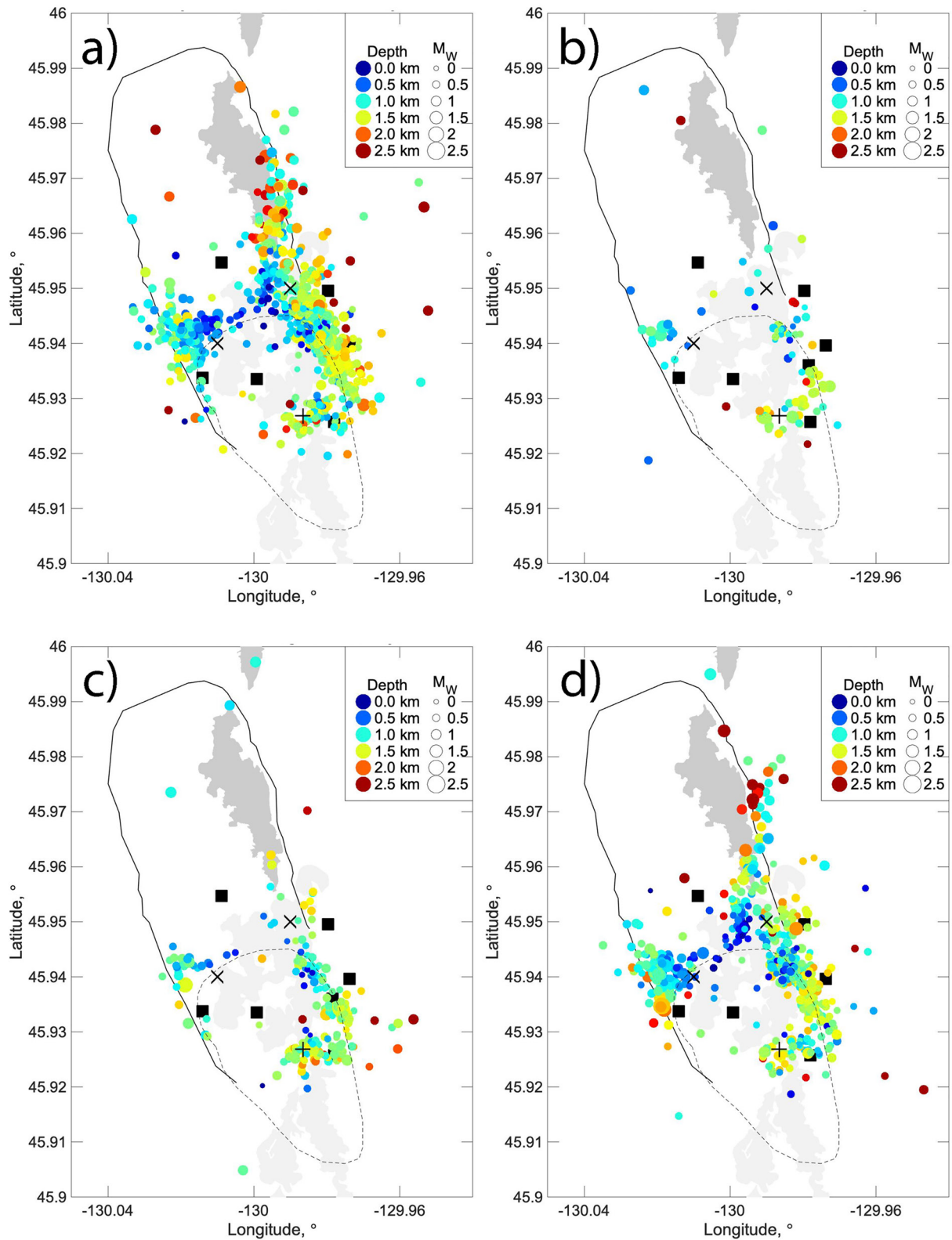


Figure 8.

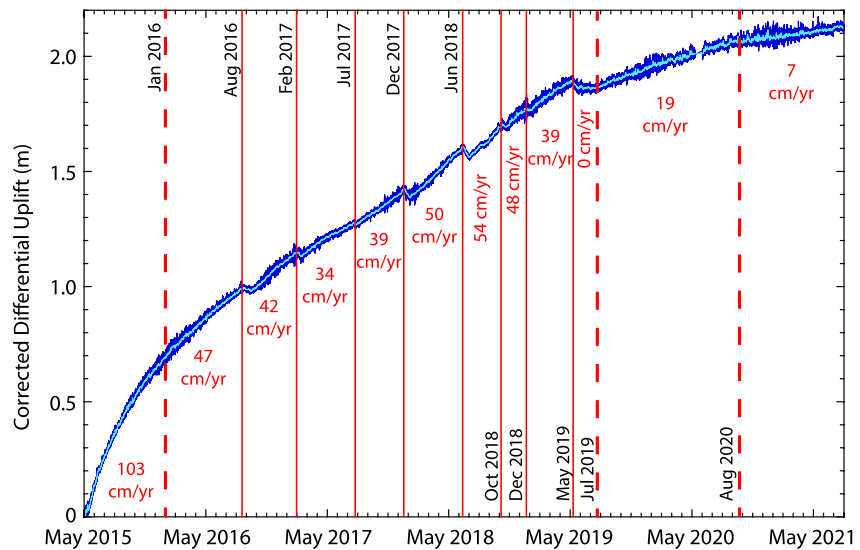


Figure 9. Plot of differential bottom pressure recorder (BPR) data (OOI-BPR-MJ03F-E) from the 2015 eruption to the present, corrected to approximate the *single-station* uplift at the caldera center by multiplying by 1.67. Dark-blue curve is data sub-sampled to every 15 min; light-blue curve is data averaged over 1-day windows. Overlain in red are average rates of uplift between (not including) each of the short-term deflation events (vertical red lines), and between other somewhat arbitrary times of apparent rate changes (vertical dashed lines). Note minor changes in rates between some short-term deflation events and major changes in rates in May 2019 and around August 2020.

the rate decreased further by about half to 19 cm/yr, and it decreased by more than half again to only 7 cm/yr between August 2020 and August 2021.

We interpret that the decreasing rate of uplift reflects a sharply waning magma supply, and the short-term deflation events observed between 2016 and 2020 may be a consequence of this waning supply. Perhaps when the driving pressure that feeds magma upward through the stacked sills to the shallow reservoir wanes, it can be temporarily insufficient to keep the conduits open that transport magma upwards, such that they close until the driving pressure builds again to re-open them and a new equilibrium supply rate is re-established. This idea is more consistent with the second of the hypotheses presented in Section 4.1 above. If true, this re-equilibration process occurred repeatedly during the time period when the deflation events were occurring and the magma supply rate was waning.

Since May 2019, we have not identified any other obvious short-term deflation events in the differential BPR record (Figures 4a and 9). Why did they stop? Perhaps the magma supply rate stabilized at a new lower level and so the temporary interruptions associated with the decreasing rate of supply stopped. Another question is whether any short-term deflation events were observed before 2015. None are obvious, but this could be because we did not have the capability to create an effective differential BPR record before 2014 when the OOI-RCA was deployed, because all the non-cabled BPRs were located too close to one another to provide an adequate reference (their rates of inflation were not different enough from each other).

Figure 8. Maps of earthquake epicenters detected before, during, and after the June 2018 short-term deflation event, color-coded by depth (see legend), showing that the spatial pattern of seismicity did not change during the event. (a) Earthquakes from the 24 days before the deflation event (21 May–14 June). (b) Earthquakes from the 18 days during the deflation event (14 June–2 July). (c) Earthquakes during the next 30 days of re-inflation (2 July–1 August). (d) Earthquakes during the next 24 days after the level of re-inflation had returned to its previous high and higher seismicity resumed (1–25 August). Arcuate outline is caldera rim, dashed outline is deep stacked sills from Carbotte et al. (2020), “+” symbol is approximate center of sills, X’s are centroids of best-fit deformation models of Nooner and Chadwick (2016) at right and Hefner et al. (2020) at left, black squares are OOI seismometer locations, light- and dark-gray areas are lava flows erupted in 2011 and 2015, respectively. Similar maps for the other short-term deflation events are provided in Supporting Information S1.

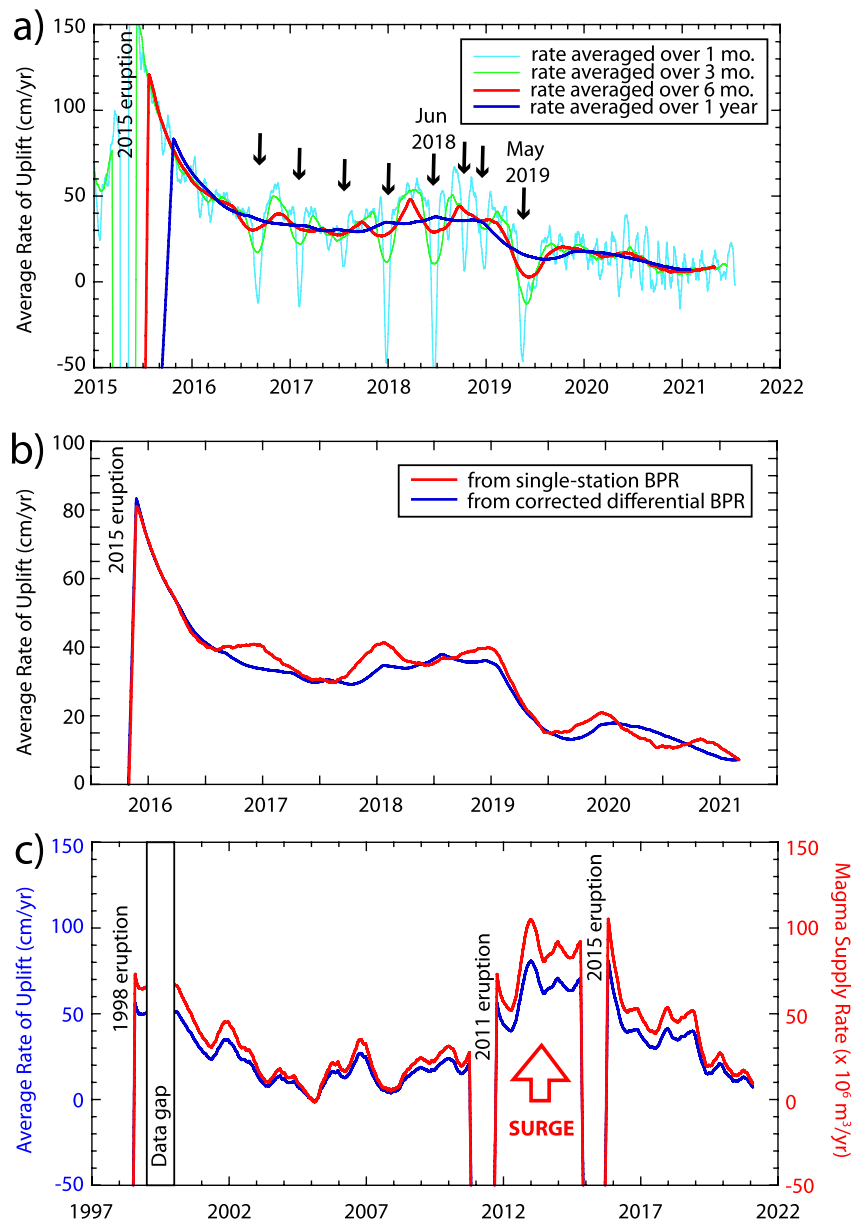


Figure 10. Variation of average rate of uplift at the caldera center and magma supply rate over time. (a) Plot showing variation in uplift rate since the 2015 eruption, derived from the differential bottom pressure recorder (BPR) record (OOI-BPR-MJ03F-E), averaged over different time periods (1 month in light-blue, 3 months in light-green, 6 months in red, and 1 year in blue). Differential BPR data are corrected to approximate the single-station uplift at the caldera center by multiplying by 1.67. Arrows show the eight identified short-term deflation events visible as dips in the uplift rate in the 1-month average curve (light-blue). (b) Plot comparing uplift rate averaged over a 1 year time window using the corrected differential BPR record (in blue) to the single-station BPR data (in red), showing good agreement. (c) Long-term plot showing variation in uplift rate from 1997 to 2022, derived from the single-station BPR record at the center of the caldera, averaged over a 1-year moving time window (blue curve, left y-axis) and magma supply rate calculated from the averaged uplift rate and the best-fit deformation model of Nooner and Chadwick (2016) (red curve, right y-axis). A surge in the magma supply occurred between the 2011–2015 eruptions.

4.3. The Long-Term Inflation Record and Changes in Magma Supply With Time

The long-term variation in uplift rate at the center of the caldera from 1997 to 2021 is shown in Figure 10, using both the corrected *differential* BPR record since 2014, and the *single-station* BPR record extending back to 1997. Figure 10a shows the variation in the uplift rate since the 2015 eruption, calculated from the corrected *differential*

BPR record, averaged over time windows of 1 month, 3 months, 6 months, and 1 year. Overall, it is clear that the rate of uplift has been decreasing sharply since the 2015 eruption. The arrows in Figure 10a show the eight identified short-term deflation events, which are visible as dips in the uplift rate in the 1-month average curve. The 1-year average curve shows longer-term trends, including a rapid decrease in uplift rate in the first 2 years after the 2015 eruption, followed by 2 years of a relatively steady rate until May 2019, when the rate suddenly decreased and it has been on a downward trend since then.

Figure 10b compares the uplift rate calculated using the corrected *differential* BPR record versus the *single-station* BPR data, both averaged over a 1-year moving time window, showing good agreement between the two. This confirms that our correction factor for the *differential* rates (multiplying by 1.67 to estimate true uplift at the caldera center) is valid and enables comparison of rates derived from the longer *single-station* BPR record. We speculate that the apparently higher uplift rates in the fall/winter of each year in the *single-station* curve in Figure 10b may be seasonal oceanographic effects that are removed from the *differential* record. Among the possible processes contributing to the seasonal signal in the single-station BPR data are stronger wind-forced bottom currents flowing over the sensors in winter versus summer (the Bernoulli effect) (Thomson et al., 1990), dynamic air-pressure forcing by Rossby-Haurwitz surface waves that may have seasonal amplitude cycles (Thomson & Fine, 2021), and pronounced seasonal shifts in circulation and water masses of the California Current System (Hickey, 1979, 1989; Lynn & Simpson, 1987).

Figure 10c shows the longer-term variation in uplift rate from 1997 to 2022, derived from the *single-station* BPR record, again averaged over a 1-year moving time window (blue curve). Of course, the rates would be higher if averaged over a shorter time window. For example, the large co-eruption deflations (which only last 1–4 weeks) effectively drown out higher rates of inflation both before and after eruptions with a 1-year averaging window. Nevertheless, Figure 10c shows that the 1-year averaged uplift rate has varied from <10 to >80 cm/yr since 1997, with the highest rates between the 2011 and 2015 eruptions.

Each centimeter of uplift can be associated with the addition of 1.3×10^6 m³ of magma into the shallow reservoir, based on the best-fit deformation model of Nooner and Chadwick (2016) (see Supporting Information S1). While these calculated supply rates are highly dependent on the deformation model, they provide a quantitative illustration of how much the supply has changed with time. The red curve in Figure 10c shows that the magma supply rate was relatively high after the 1998 eruption (30 – 60×10^6 m³/yr), it decreased until it reached a low in 2005 ($<10 \times 10^6$ m³/yr), then it gradually increased again leading up to the 2011 eruption (20 – 30×10^6 m³/yr). After the 2011 eruption, the rate was substantially higher (55 – 100×10^6 m³/yr) and even increased leading up to the 2015 eruption. Since then, the rate has decreased rapidly as discussed above.

Looking at this long-term view, it becomes clear that there was a surge in the magma supply rate to Axial between the 2011 and 2015 eruptions. This would explain why those two eruptions were so close together in time (Chadwick et al., 2016), and shows that the eruption recurrence interval at Axial depends strongly on the underlying rate of magma supply (Nooner & Chadwick, 2016). Figure 10c also shows that the recent decrease in rates is similar to the post-1998 eruption time period. The overall long-term pattern approximates a sinusoidal curve of decreasing and increasing rates with a wavelength of about a decade, and a magma supply amplitude that varies by about an order of magnitude (from $<10 \times 10^6$ to $>100 \times 10^6$ m³/yr). This raises the possibility that the current relatively low magma supply rate will turn around and start increasing again in the coming years.

4.4. Implications for Eruption Forecasting

The waning magma supply has implications for eruption forecasting (based solely on pattern recognition and the assumption of a critical level of inflation/pressure). Because the eruptions at Axial Seamount appear to be “inflation-predictable” (Nooner & Chadwick, 2016) and there are no negative consequences for false alarms since no humans live nearby, we have been experimenting with various methods for extrapolating the rate of inflation into the future to aid in eruption forecasting. The method that currently seems the most robust is to use the *differential* OOI-BPR uplift rate averaged over the previous 6 months to extrapolate into the future (Figure 11a). From that, we calculate the date that the volcano will reach the 2015 inflation threshold, and the date for a level of inflation 20 cm higher (since the 2015 eruption was triggered at a *single-station* level 30 cm higher than the 2011 eruption, and the *differential* inflation values are about 2/3 of the *single-station* values). Using continuous real-time data from the OOI cabled observatory, we make these extrapolations once a day, so they vary with time,

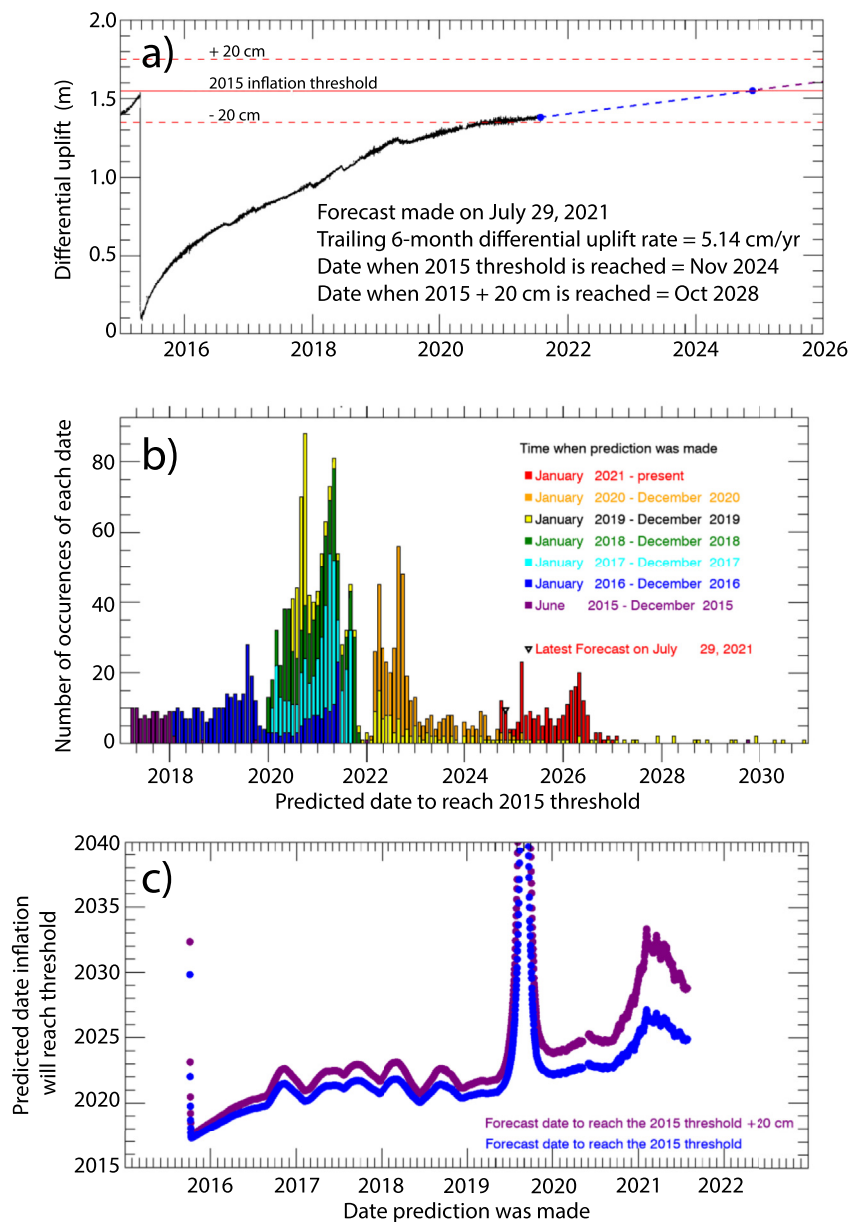


Figure 11. Inflation threshold forecast plots. (a) Plot of differential bottom pressure recorder (BPR) data (OOI-BPR-MJ03F-E; black curve) showing re-inflation since the 2015 eruption. A blue dashed line extrapolates into the future using the average rate of inflation from the previous 6 months; blue dot is date when 2015 inflation threshold is reached (see legend). (b) Histogram of predicted dates when inflation will reach the 2015 threshold, color coded by when the predicted date was calculated, based on the average rate of re-inflation from the previous 6 months, beginning in June 2015. Predicted dates are binned in months. (c) Plot of predicted date that inflation will reach the 2015 inflation threshold (Y-axis) versus date on which the prediction was made (X-axis). Blue dots are date to reach the 2015 inflation threshold; purple dots are for a threshold 20 cm higher. Note predicted dates were earliest when the rate of re-inflation was highest soon after the 2015 eruption (left side of plot). Peaks in the curves show time periods when the average rate of inflation slowed significantly (especially in mid-2019), which pushed the predicted dates farther into the future.

depending on the recent inflation rate. Figure 11b shows a histogram of the predicted dates that Axial would reach the 2015 inflation threshold, made daily since the 2015 eruption, color-coded as a function of time. This shows that as the rate of inflation slowed with time, the predicted date when the volcano would reach the 2015 inflation threshold has moved farther into the future. Another way of showing this is in Figure 11c, in which the predicted date of reaching the 2015 threshold (on the y-axis) is plotted against the date that the prediction was

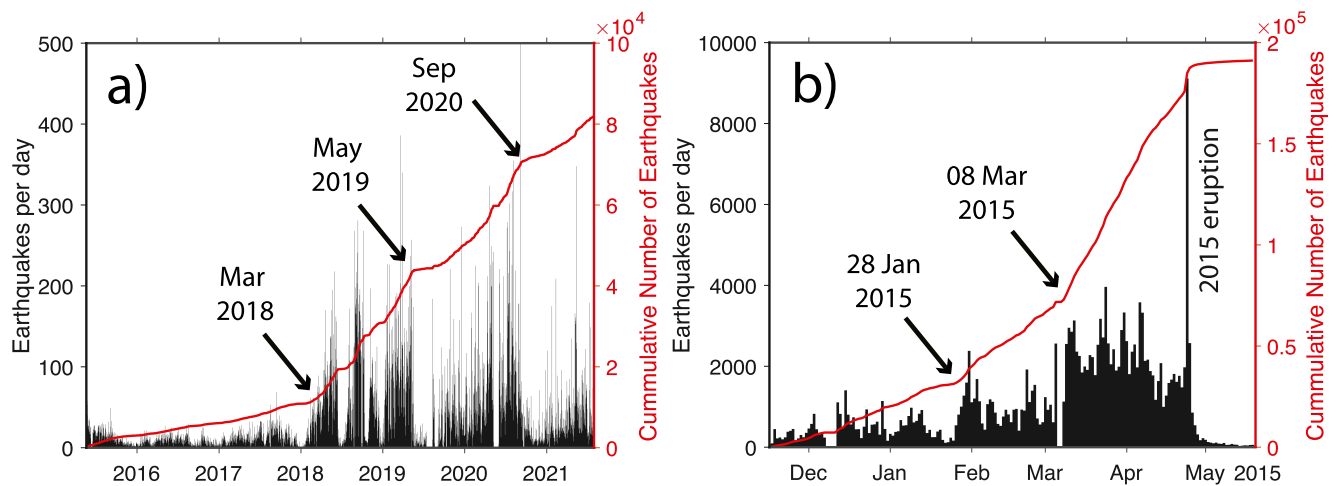


Figure 12. Histograms of earthquakes per day (black bars) and cumulative number of earthquakes (red curves) over time based on OOI data. (a) Seismicity since the 2015 eruption. (b) Seismicity before the 2015 eruption. Arrows point to times of significant changes in the rate of earthquakes.

made (on the x -axis). The blue curve is for the 2015 threshold and the purple curve is for an inflation level 20 cm higher. Both Figures 11b and 11c show that the predicted dates were earlier than 2020 from the end of 2015 until mid-2016 when the rate of re-inflation was high. Then as the rate of re-inflation stabilized at a lower level, the predicted dates moved into the 2020–2022 range from mid-2016 to mid-2019. The undulations in the curves in Figure 11c during this interval are due to the short-term deflation events, each of which temporarily moved the predicted dates forward in time. The May 2019 short-term deflation event caused a major perturbation, moving the predicted dates far into the future temporarily (shown by the spike in predicted dates in Figure 11c), when the inflation rate approached zero. Afterward, the predicted dates settled down in the 2022–2024 range between mid-2019 to late-2020, due to the lower inflation rate after May 2019. Then after August 2020, the predicted dates moved sharply into the future again as the inflation rate slowed further. Similar plots are updated daily with the latest OOI-BPR data at this URL: <https://www.pmel.noaa.gov/eoi/rsn/Forecasts4.html>.

We have used this information to make subjective eruption forecast windows that are periodically revised based on the latest data. A blog of our eruption forecast efforts is kept at this URL: https://www.pmel.noaa.gov/eoi/axial_blog.html. In addition, we might expect the next eruption to require a somewhat higher inflation threshold (and magmatic pressure), because the historical eruptions at Axial have intruded dikes in both rift zones, and it may take some time for plate spreading to increase the extensional stresses along the rifts again. In any case, because of the real-time geodetic and seismic data available from the OOI-RCA, we can continually adjust the eruption forecast outlook, as rates of inflation and seismicity change. For now, the next eruption appears to be at least 4 years away, consistent with the current relatively low rates of seismicity (Figure 12a), compared to the rates observed just before the 2015 eruption (Figure 12b). Therefore, the interval between the 2015 eruption and the next one will likely be more like the 13-year interval between the 1998–2011 eruptions, than the 4-year interval between the 2011–2015 eruptions.

4.5. Changes in Magma Supply at Other Basaltic Volcanoes

The reason that the shallow magma supply at Axial Seamount has varied with time presumably reflects changes in the deep supply from the mantle source region. Similar volcanic settings where continuous inflation data over several decades can be used to quantify a varying magma supply rate are somewhat rare. Kilauea volcano, Hawaii, is one example where Poland et al. (2012) showed that the rate of magma supply approximately doubled between 2003 and 2007, from 0.11 to at least 0.19 km³/yr, during a time when the volcano was erupting continuously. They interpreted that the surge originated in the mantle and showed how it was manifested at the surface by changes in eruption rate, gas emission, seismicity, and deformation. While the pre-surge magma supply rate at Axial is about an order of magnitude lower than at Kilauea, the relative magnitude of the surge at Axial was greater than at Kilauea (~10 times larger vs. ~2 times larger), and during Axial's recent surge the magma supply approached Kilauea's background rate.

Another basaltic hotspot volcano with a well-documented long-term inflation record and demonstrated variations in magma supply is Sierra Negra volcano in the Galápagos. Here, deformation monitoring since 1992 by InSAR, campaign-GPS, and continuous-GPS shows that inflation rates have varied considerably over several decades. After 8 years of inflation between 1992 and 1999, several years of little or no inflation followed in 1999–2003, which gave way to a period of rapidly accelerating uplift that led up to the 2005 eruption, eventually amounting to ~5 m of uplift since 1992 (Chadwick, Geist, et al., 2006; Geist et al., 2008). Following 5.4 m of co-eruption deflation in 2005 (Yun et al., 2007), Sierra Negra re-inflated more than 6.5 m before its next eruption in 2018 (Bell, Femina, et al., 2021; Bell, Hernandez, et al., 2021; Vasconez et al., 2018). This time, the inter-eruption period included five distinct time periods with varying rates of inflation or minor deflation (Bell, Femina, et al., 2021; Bell, Hernandez, et al., 2021). The surface deformation at Sierra Negra is best fit by increased pressure in a sill-like shallow magma reservoir 2 km below the caldera floor (Amelung et al., 2000; Chadwick, Geist, et al., 2006; Jónsson, 2009; Yun et al., 2006). However, geobarometric analyses from the 2018 lavas suggest there is a second reservoir at 7.5 km depth (Bell, Femina, et al., 2021). Thus, the varying rates of inflation can be interpreted as variations in pressure (and supply) between the shallow and deeper reservoirs (Bell, Hernandez, et al., 2021).

Piton de la Fournaise is another intraplate basaltic hotspot volcano on the island of Reunion in the Indian Ocean where long-term inflation/deflation has been observed over multiple eruption cycles. Peltier et al. (2008) presented monitoring data from a very active period in 2004–2006 that included six eruptions. The volcano inflated between some of these eruptions, but at varying rates, and some inflation episodes were separated by periods of minor deflation. The source of the deformation was modeled as a single source at a depth of ~2.3 km below the summit (Peltier et al., 2008). They interpreted these as cycles of magma supply into and out of the shallow reservoir from a deeper reservoir below, with a quasi-continuous (but varying) magma supply. Over a longer time period, a review of monitoring data since 1972 by Peltier et al. (2009) suggests that the magma supply from the mantle has been more intermittent with periods of no significant inflation separating periods of active recharge with multiple eruption cycles, and a more regular supply since 2000.

These examples show that magma supply at oceanic basaltic volcanoes influenced by hotspots can change significantly over time periods of months to years and that such changes (both increases and decreases) are common. With this perspective, the variations we have documented at Axial Seamount are not unusual, and we should perhaps expect to see the magma supply rate increase again before its next eruption.

4.6. Relationship Between Deformation and Seismicity

Building on the work of Voight (1988), Kilburn (2012, 2018) developed a rock-mechanics based physical model to explain how surface uplift and elevated seismicity co-vary with time between eruptions at closed-system caldera-volcanoes. In the model, seismicity and uplift are viewed as proxies for the inelastic and total deformation of a crust, respectively, and the inelastic deformation is accommodated on a dispersed population of small faults. The model predicts that the rate of seismicity depends on both the uplift rate and the total uplift during an eruption cycle, as a volcano evolves through *elastic*, *quasi-elastic*, and *inelastic* deformation regimes (Bell, Hernandez, et al., 2021; Kilburn, 2018). In the *elastic* and early *quasi-elastic* regimes at the beginning of a cycle, the rate of seismicity is low even though the rate of uplift can be high, because the cumulative deformation and crustal stress state are low (after stress relaxation during the previous eruption). As the total uplift accumulates during re-inflation and differential stresses increase, the model predicts that the number of earthquakes per unit of uplift should increase exponentially with total uplift in the *quasi-elastic* regime, as small fault patches become progressively stressed and begin to accommodate some of the deformation. The seismicity represents the small but growing component of inelastic deformation and damage accumulation in the crust. Once a critical stress threshold is reached, the deformation enters an *inelastic* regime in which most of the deformation is accommodated by brittle failure and fault slip, and both the rate of earthquakes and deformation may increase hyperbolically, leading to failure in the shallow crust between the magma reservoir and the surface, producing an eruption. However, in some cases, a period of constant-rate seismicity and deformation occurs before, or instead of, the hyperbolic phase in the *inelastic* regime (Bell, Hernandez, et al., 2021; Kilburn, 2018).

This elastic-to-brittle physical model has been successfully applied to explain inter-eruption monitoring data at a variety of basaltic caldera volcanoes, including Kilauea, Hawaii (Bell & Kilburn, 2012) and Sierra Negra, Galápagos (Bell, Hernandez, et al., 2021), as well as at silicic calderas with long and complex periods of unrest, such as Rabaul, Papua New Guinea (Robertson & Kilburn, 2016) and Campi Flegrei, Italy (Kilburn et al., 2017).

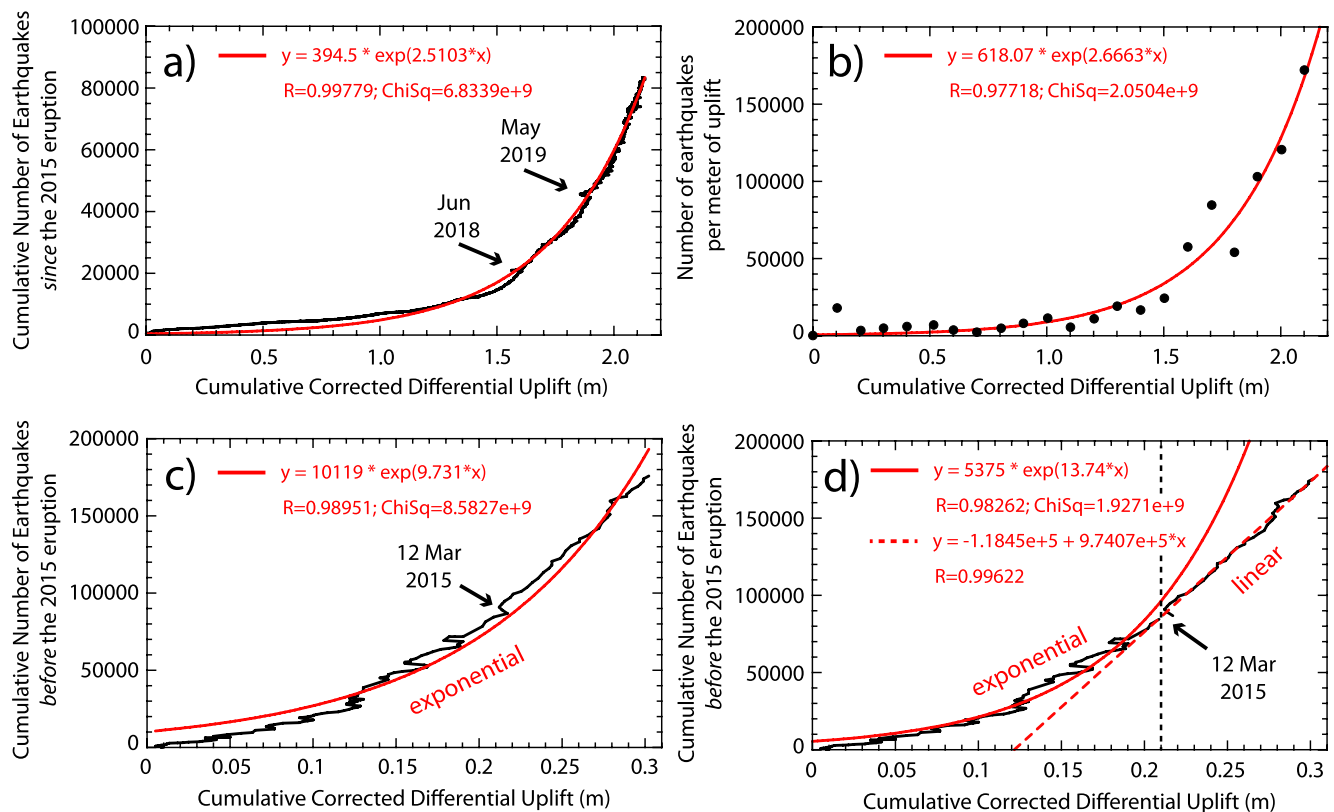


Figure 13. Plots showing exponential relationship between rates of seismicity and deformation. (a) Black curve is cumulative number of earthquakes versus total uplift since the 2015 eruption (1 May 2015 to 1 August 2021). Red curve is best-fitting exponential equation. (b) Earthquake rate per meter of uplift since the 2015 eruption (1 May 2015 to 1 August 2021), showing that it also follows an exponential relationship (red curve). (c) Cumulative number of earthquakes versus total uplift *before* the 2015 eruption, starting when the OOI cabled observatory became operational (16 November 2014 to 23 April 2015). In this plot the data (black curve) are compared to an exponential curve (red curve) over the entire period. (d) Same data as in (c) but separated into two time periods before and after 12 March 2015 (vertical dashed line), and fit to an exponential curve before (solid red line) and to a linear curve after (red dashed line), which could indicate an increasing component of inelastic deformation precursory to the eruption. In all plots, the X-axis is cumulative differential uplift (OOI-BPR-MJ03F-E), corrected to approximate actual uplift at the caldera center by multiplying by 1.67.

As seen in the previous section, the behavior of Sierra Negra in particular (Bell, Hernandez, et al., 2021) has many parallels to Axial Seamount, and the elastic-to-brittle model appears to fit the observations at both volcanoes quite well. At both volcanoes, there appears to be little or no *elastic* phase and instead an eruption cycle starts right into the *quasi-elastic* phase with seismicity accompanying deformation.

Figure 13a shows the cumulative number of earthquakes as a function of total uplift at Axial Seamount since the 2015 eruption. In the first few years, the number of earthquakes per unit uplift was low but it has gradually increased with time such that the cumulative earthquakes to total uplift curve fits an exponential trend rather well (Figure 13a), as predicted by the *quasi-elastic* phase of Kilburn (2018). The increasing number of earthquakes represent an increasing proportion of the deformation being accommodated by inelastic deformation, although the bulk of the deformation remains elastic and slip on the caldera faults is still a minor contributor to the overall strain. Another way of showing this is a plot of the number of earthquakes per meter of uplift since the 2015 eruption, which also follows an exponential relationship (Figure 13b). Seismicity rate is an effective proxy for inelastic strain at Axial because it is dominated by small-magnitude earthquakes and larger events are rare.

At Sierra Negra volcano, Bell, Hernandez, et al. (2021) showed similar relationships between seismicity and deformation between its 2005 and 2018 eruptions. However, in addition they found that in the final 6 months before the 2018 eruption, the number of earthquakes per unit of uplift stopped following an exponential trend and changed to a constant linear trend instead. This was interpreted as the end of the *quasi-elastic* phase and the beginning of the *steady-inelastic* phase of Kilburn (2018), when the differential stress reached a critical failure value. We may see a similar pattern before the 2015 eruption at Axial Seamount, but it is less obvious. Figures 13c

and 13d show the cumulative number of earthquakes versus total uplift in the final 5 months before the 2015 eruption (note that the totals only reflect the number of earthquakes and the amount of uplift after 16 November 2014, when the seismometers on the OOI cabled observatory became operational). It is ambiguous whether the curve follows an exponential pattern all the way up to the eruption (Figure 13c), or whether it is exponential until around 12 March 2015 and then becomes linear during the final 1.5 months before the eruption (Figure 13d). The data can be reasonably fit either way, perhaps because of the limited time period. Before the next eruption at Axial, it may be more evident whether a shift from exponential to linear occurs, because we will have monitoring data over an entire eruption cycle for the first time. Such a transition may signal that the crust surrounding the magma reservoir is becoming critically stressed and is approaching failure (Cabaniss et al., 2020).

The elastic-to-brittle physical model also provides another potential method for forecasting the timing of the next eruption at Axial Seamount. The current rate of earthquakes per meter of uplift is $\sim 1.7 \times 10^5 \text{ m}^{-1}$ (Figure 13b), which is about 17% of the rate of $\sim 10^6 \text{ m}^{-1}$ seen in the 6 weeks prior to the 2015 eruption (Figure 13d). Assuming a similar threshold for the rate of earthquakes with uplift for the next eruption, the exponential model in Figure 13a would predict that Axial will erupt again when the corrected differential uplift reaches $\sim 2.8 \text{ m}$, or $\sim 0.7 \text{ m}$ above its current level of $\sim 2.1 \text{ m}$ (Figure 9). Since the 2015 eruption was triggered when the corrected differential uplift was $\sim 2.4 \text{ m}$, that inflation threshold would be $\sim 0.4 \text{ m}$ higher than for the 2015 eruption, similar to the 0.3 m higher threshold in 2015 compared to 2011. Given that the current rate of inflation is only $\sim 7 \text{ cm/yr}$, this prediction is also consistent with the inference above that the next eruption is still years away.

The model of Kilburn (2018) helps explain how a low rate of seismicity can accompany a high rate of post-eruption uplift early in Axial's inter-eruption cycle, and yet later in the cycle a lower rate of uplift is associated with a higher rate of seismicity (because the total uplift, accumulated strain, and differential stress are all higher). It also successfully predicts that the number of earthquakes per unit of uplift during the inter-eruption period increases exponentially with total uplift. Continued monitoring will show whether pattern recognition and a repeatable critical inflation threshold continues to be an effective way to forecast eruptions at Axial Seamount, or whether changes in the trends of earthquakes per unit of uplift may be a better way to anticipate the timing of failure around the shallow magma reservoir as a precursor to eruption.

5. Conclusions

As of mid-2021, Axial Seamount has re-inflated 85%–90% of the deflation it experienced during its last eruption in 2015. However, the long-term rate of inflation has been gradually decreasing since 2015. By using differential BPR data (subtracting data from a reference station to remove oceanographic noise and enhance the geodetic signal), we identified eight repeated short-term deflation events between August 2016 and May 2019, each associated with a simultaneous drop in seismicity, and some with changes in the average inflation rate. We interpret these as either small movements of magma out of the shallow reservoir or interruptions to the magma supply that may be a consequence of a waning supply from the mantle since the 2015 eruption. The long-term geodetic record suggests that variations in the magma supply rate of about an order of magnitude occur at Axial over decadal time scales, and the current supply rate is ~ 10 times less than a surge that fed the closely spaced 2011 and 2015 eruptions. This variation of magma supply from depth over a period of years appears to be common at other basaltic hotspot-influenced volcanoes, and we should anticipate further changes. The decrease in inflation rate since the 2015 eruption has implications for eruption forecasting and our current forecast window is wide and poorly constrained, between 2025 and 2030, but could change as the rate of inflation continues to vary. This shows that the eruption recurrence interval at Axial strongly depends on the magma supply rate, and that the interval between Axial's last and next eruptions is likely to be closer to the 13 years between 1998 and 2011, rather than the 4 years between 2011 and 2015.

The rates of seismicity and deformation since the 2015 eruption at Axial show that they are tightly linked and covary such that the cumulative number of earthquakes increases exponentially with total uplift, due to the increase of differential stress in the crust overlying the shallow magma reservoir caused by magma accumulation. The data are consistent with a physical model of cumulative damage in the crust at volcanoes undergoing inter-eruption re-inflation that increases the component of inelastic deformation with time (the seismicity relative to the total uplift) until a critical overpressure threshold is reached that triggers tensile failure at the margin of the reservoir, culminating in dike propagation and eruption at the surface. Extrapolating the current earthquake rates based on

the exponential relationship to total uplift and comparison to the 2015 eruption provides another basis for eruption forecasting. Real-time monitoring data from the OOI cabled observatory at Axial will allow us to compare the effectiveness of eruption forecasts based on the repeating pattern of deformation alone, the exponential model of earthquake rates to total uplift, and recognizing a transition from exponential to linear in the trend of earthquakes to total uplift that may signal imminent failure in the crust between the shallow magma reservoir and the surface. In sum, Axial Seamount continues to serve as an outstanding natural laboratory for better understanding the active volcanic processes that lead to eruptions.

Data Availability Statement

The data presented here are from OOI Bottom Pressure Tilt instruments (RS03CCAL-MJ03F-BOTPTA301 and RS03ECAL-MJ03E-BOTPTA302), using data from 30 August 2014 to 1 August 2021. The data are archived at the NSF OOI Data Portal at <https://ooinet.oceanobservatories.org> and <https://dataexplorer.oceanobservatories.org>. Non-cabled pressure data sets are archived at the Marine Geoscience Data System at: https://www.marine-geo.org/tools/search/entry.php?id=JdF:Axial_Deformation (Chadwick & Nooner, 2015; Fox, 2016). The OOI seismic data are archived at the Incorporated Research Institutions for Seismology Data Management System (IRIS), <https://www.iris.edu/> and <http://fdsn.adc1.iris.edu/networks/detail/OO/>. A catalog of seismic data are archived at the Marine Geoscience Data System (Wilcock et al., 2017) and are also available at <http://axial.ocean.washington.edu/>.

Acknowledgments

This paper uses data provided by the Ocean Observatories Initiative (OOI), which is a major facility fully funded by the National Science Foundation (NSF). This research was also supported by NSF awards OCE-1356839 and 1736882 to W. W. Chadwick and S. L. Nooner, awards OCE-1634150 and 1928282 to W. W. Chadwick, and award OCE-1536219 to W. S. D. Wilcock. Additional support was provided by the National Oceanic and Atmospheric Administration, Pacific Marine Environmental Laboratory, Earth-Ocean Interactions Program. The authors are grateful for the outstanding logistical support at sea provided by the crews of *R/V Thompson* and *ROV Jason*. This work would not have been possible without the hard work of the University of Washington OOI Regional Cabled Array team, led Deborah Kelley and pioneered by John Delaney. The paper benefited from helpful comments by Del Bohnenstiehl and two anonymous reviewers. PMEL contribution #5321.

References

- Acocella, V. (2007). Understanding caldera structure and development: An overview of analogue models compared to natural calderas. *Earth-Science Reviews*, 85, 125–160. <https://doi.org/10.1016/j.earscirev.2007.08.004>
- Amelung, F., Jónsson, S., Zebker, H., & Segall, P. (2000). Widespread uplift and 'trapdoor' faulting on Galápagos volcanoes observed with radar interferometry. *Nature*, 407, 993–996. <https://doi.org/10.1038/35039604>
- Anderson, A. N., Foster, J. H., & Frazer, N. (2020). Implications of deflation-inflation event models on Kīlauea Volcano, Hawai'i. *Journal of Volcanology and Geothermal Research*, 397, 106832. <https://doi.org/10.1016/j.jvolgeores.2020.106832>
- Anderson, K. R., Poland, M. P., Johnson, J. H., & Miklius, A. (2015). Episodic deflation-inflation events at Kīlauea Volcano and implications for the shallow magma system. In R. Carey, V. Cayol, M. Poland, & D. Weis (Eds.), *Hawaiian volcanism: From source to surface* (Vol. 208, pp. 229–250). American Geophysical Union Geophysical Monograph Series. <https://doi.org/10.1002/9781118872079.ch11>
- Arnulf, A. F., Harding, A. J., Kent, G. M., Carbotte, S. M., Canales, J. P., & Nedimovic, M. R. (2014). Anatomy of an active submarine volcano. *Geology*, 42(8), 655–658. <https://doi.org/10.1130/G35629.1>
- Arnulf, A. F., Harding, A. J., Kent, G. M., & Wilcock, W. S. D. (2018). Structure, seismicity, and accretionary processes at the hotspot-influenced Axial Seamount on the Juan de Fuca Ridge. *Journal of Geophysical Research*, 123, 4618–4646. <https://doi.org/10.1029/2017JB015131>
- Arnulf, A. F., Harding, A. J., Sastrup, S., Kell, A., Kent, G. M., Carbotte, S. M., et al. (2019). Imaging the internal workings of Axial Seamount on the Juan de Fuca Ridge. In *Abstract OS51B-1483 presented at 2019 Fall Meeting, AGU, San Francisco, CA, 9–13 December*.
- Arnulf, A. F., Sastrup, S., Eischen, T., Harding, A. J., Kent, G. M., Carbotte, S. M., et al. (2020). Seismic imaging of the internal workings of Axial Seamount on the Juan de Fuca Ridge. In *Abstract V043-05 presented at 2020 Fall Meeting, AGU, San Francisco, CA, 7–11 December*.
- Baillard, C., Wilcock, W. S. D., Arnulf, A. F., Tolstoy, M., & Waldhauser, F. (2019). A joint inversion for three-dimensional P and S wave velocity structure and earthquake locations beneath Axial Seamount. *Journal of Geophysical Research: Solid Earth*, 124, 12997–13020. <https://doi.org/10.1029/2019JB017970>
- Battaglia, M., Cervelli, P. F., & Murray, J. R. (2013). dMODELS: A MATLAB software package for modeling crustal deformation near active faults and volcanic centers. *Journal of Volcanology and Geothermal Research*, 254, 1–4. <https://doi.org/10.1016/j.jvolgeores.2012.12.018>
- Bell, A. F., Femina, P. C. L., Ruiz, M., Amelung, F., Bagnardi, M., Bean, C. J., et al. (2021). Caldera resurgence during the 2018 eruption of Sierra Negra volcano, Galápagos Islands. *Nature Communications*, 12(1), 1397. <https://doi.org/10.1038/s41467-021-21596-4>
- Bell, A. F., Hernandez, S., Femina, P. C. L., & Ruiz, M. C. (2021). Uplift and seismicity driven by magmatic inflation at Sierra Negra Volcano, Galápagos Islands. *Journal of Geophysical Research: Solid Earth*, 126, e2021JB022244. <https://doi.org/10.1029/2021JB022244>
- Bell, A. F., & Kilburn, C. R. J. (2012). Precursors to dyke-fed eruptions at basaltic volcanoes: Insights from patterns of volcano-tectonic seismicity at Kīlauea volcano, Hawaii. *Bulletin of Volcanology*, 74(2), 325–339. <https://doi.org/10.1007/s00445-011-0519-3>
- Cabaniss, H. E., Gregg, P. M., Nooner, S. L., & Chadwick, W. W., Jr. (2020). Triggering of eruptions at Axial Seamount, Juan de Fuca Ridge. *Scientific Reports*, 10, 10219. <https://doi.org/10.1038/s41598-020-67043-0>
- Caplan-Auerbach, J., Dziak, R. P., Haxel, J., Bohnenstiehl, D. R., & Garcia, C. (2017). Explosive processes during the 2015 eruption of Axial Seamount, as recorded by seafloor hydrophones. *Geochemistry, Geophysics, Geosystems*, 18, 1761–1774. <https://doi.org/10.1002/2016GC006734>
- Carbotte, S. M., Arnulf, A. F., Spiegelman, M. W., Lee, M., Harding, A. J., Kent, G. M., et al. (2020). Stacked sills forming a deep melt-mush feeder conduit beneath Axial Seamount. *Geology*, 48, 693–697. <https://doi.org/10.1130/G47223.1>
- Caress, D. W., Clague, D. A., Paduan, J. B., Chadwick, W. W., Jr., Nooner, S. L., & Thomas, H. J. (2020). Vertical deformation of the Axial Seamount Summit from Repeated 1-m scale bathymetry surveys using AUVs. In *Abstract V040-0017 presented at 2020 Fall Meeting, AGU, San Francisco, CA, 7–11 December*.
- Caress, D. W., Clague, D. A., Paduan, J. B., Martin, J., Dreyer, B., Chadwick, W. W., Jr., et al. (2012). Repeat bathymetric surveys at 1-metre resolution of lava flows erupted at Axial Seamount in April 2011. *Nature Geoscience*, 5(7), 483–488. <https://doi.org/10.1038/NGEO1496>
- Caress, D. W., Clague, D. A., Paduan, J. B., Thomas, H., Chadwick, W. W., Jr., Nooner, S. L., & Yoerger, D. R. (2015). Vertical deformation of the Axial Seamount summit from repeated 1-m scale bathymetry surveys with AUVs. Abstract presented at 2015 Annual GSA Meeting, Baltimore, MD, 1–4 November. *GSA Abstracts with Programs*, 47(7).

- Caress, D. W., Clague, D. A., Paduan, J. B., Thomas, H. J., Chadwick, W. W., Jr., Nooner, S. L., & Yoerger, D. R. (2016). Vertical deformation of the Axial Seamount summit from repeated 1-m scale bathymetry surveys using AUVs. In *Abstract OS41C-1991 presented at 2016 Fall Meeting, AGU, San Francisco, Calif., 12–16 December*.
- Chadwick, J., Perfit, M., Ridley, I., Jonasson, I., Kamenov, G., Chadwick, W. W., Jr., et al. (2005). Magmatic effects of the Cobb hotspot on the Juan de Fuca Ridge. *Journal of Geophysical Research: Solid Earth*, *110*, B03101. <https://doi.org/10.1029/2003JB002767>
- Chadwick, W. W., Jr., Clague, D. A., Embley, R. W., Perfit, M. R., Butterfield, D. A., Caress, D. W., et al. (2013). The 1998 eruption of Axial Seamount: New Insights on submarine lava flow emplacement from high-resolution mapping. *Geochemistry, Geophysics, Geosystems*, *14*(10), 3939–3968. <https://doi.org/10.1002/ggge.20202>
- Chadwick, W. W., Jr., Geist, D. J., Jónsson, S., Poland, M., Johnson, D. J., & Meertens, C. M. (2006). A volcano bursting at the seams: Inflation, faulting, and eruption at Sierra Negra volcano, Galápagos. *Geology*, *34*(12), 1025–1028. <https://doi.org/10.1130/G22826A.1>
- Chadwick, W. W., Jr., & Nooner, S. L. (2015). *Processed bottom pressure recorder (BPR) data from uncabled instruments deployed at Axial Seamount on the Juan de Fuca Ridge (investigators William Chadwick and Scott Nooner)*. Integrated Earth Data Applications (IEDA). <https://doi.org/10.1594/IEDA/322282>
- Chadwick, W. W., Jr., Nooner, S. L., Butterfield, D. A., & Lilley, M. D. (2012). Seafloor deformation and forecasts of the April 2011 eruption at Axial Seamount. *Nature Geoscience*, *5*(7), 474–477. <https://doi.org/10.1038/NGEO1464>
- Chadwick, W. W., Jr., Nooner, S. L., Zumberge, M., Embley, R. W., & Fox, C. G. (2006). Vertical deformation monitoring at Axial Seamount since its 1998 eruption using deep-sea pressure sensors. *Journal of Volcanology and Geothermal Research*, *150*, 313–327. <https://doi.org/10.1016/j.jvolgeores.2005.07.006>
- Chadwick, W. W., Jr., Paduan, B. P., Clague, D. A., Dreyer, B. M., Merle, S. G., Bobbitt, A. M., et al. (2016). Voluminous eruption from a zoned magma body after an increase in supply rate at Axial Seamount. *Geophysical Research Letters*, *43*, 12063–12070. <https://doi.org/10.1002/2016GL071327>
- Clague, D. A., Paduan, J. B., Caress, D. W., Chadwick, W. W., Jr., Saout, M. L., Dreyer, B., & Portner, R. (2017). High-resolution AUV mapping and targeted ROV observations of three historical lava flows at Axial Seamount. *Oceanography*, *30*(4), 82–99. <https://doi.org/10.5670/oceanog.2017.426>
- Clague, D. A., Paduan, J. B., Dreyer, B. M., Chadwick, W. W., Jr., Rubin, K. R., Perfit, M. R., & Fundis, A. T. (2018). Chemical variations in the 1998, 2011, and 2015 lava flows from Axial Seamount, Juan de Fuca Ridge: Cooling during ascent, lateral transport, and flow. *Geochemistry, Geophysics, Geosystems*, *19*, 2915–2933. <https://doi.org/10.1029/2018GC007708>
- Cook, M. J., Sasagawa, G. S., & Zumberge, M. A. (2019). Drift corrected pressure time series at Axial Seamount, July 2018 to present. In *Abstract OS51B-1488 presented at 2019 Fall Meeting, AGU, San Francisco, CA, 9–13 December*.
- Dobashi, Y., & Inazu, D. (2021). Improving detectability of seafloor deformation from bottom pressure observations using numerical ocean models. *Frontiers of Earth Science*, *8*, 621. <https://doi.org/10.3389/feart.2020.598270>
- Dziak, R. P., & Fox, C. G. (1999). Long-term seismicity and ground deformation at Axial Volcano, Juan de Fuca Ridge. *Geophysical Research Letters*, *26*(24), 3641–3644. <https://doi.org/10.1029/1999gl002326>
- Dziak, R. P., Haxel, J. H., Bohnenstiehl, D. R., Chadwick, W. W., Jr., Nooner, S. L., Fowler, M. J., et al. (2012). Seismic precursors and magma ascent before the April 2011 eruption at Axial Seamount. *Nature Geoscience*, *5*(7), 478–482. <https://doi.org/10.1038/NGEO1490>
- Embley, R. W., Chadwick, W. W., Jr., Clague, D., & Stakes, D. (1999). The 1998 eruption of axial volcano: Multibeam anomalies and seafloor observations. *Geophysical Research Letters*, *26*(23), 3425–3428. <https://doi.org/10.1029/1999GL002328>
- Embley, R. W., Murphy, K. M., & Fox, C. G. (1990). High resolution studies of the summit of Axial Volcano. *Journal of Geophysical Research*, *95*, 12785–12812. <https://doi.org/10.1029/jb095ib08p12785>
- Fox, C. G. (1990). Evidence of active ground deformation on the mid-ocean ridge: Axial Seamount, Juan de Fuca Ridge, April–June, 1988. *Journal of Geophysical Research*, *95*, 12813–12822. <https://doi.org/10.1029/jb095ib08p12813>
- Fox, C. G. (1993). Five years of ground deformation monitoring on Axial Seamount using a bottom pressure recorder. *Geophysical Research Letters*, *20*(17), 1859–1862. <https://doi.org/10.1029/93gl01216>
- Fox, C. G. (1999). In situ ground deformation measurements from the summit of Axial Volcano during the 1998 volcanic episode. *Geophysical Research Letters*, *26*(23), 3437–3440. <https://doi.org/10.1029/1999gl000491>
- Fox, C. G. (2016). Processed bottom pressure recorder (BPR) data from uncabled instruments deployed at Axial Seamount on the Juan de Fuca Ridge (investigator Chris Fox). *Integrated Earth Data Applications (IEDA)*. <https://doi.org/10.1594/IEDA/322344>
- Fredrickson, E. K., Wilcock, W. S. D., Schmidt, D. A., MacCready, P., Roland, E., Kurapov, A. L., et al. (2019). Optimizing sensor configurations for the detection of slow-slip earthquakes in seafloor pressure records, using the Cascadia subduction zone as a case study. *Journal of Geophysical Research: Solid Earth*, *124*, 13504–13531. <https://doi.org/10.1029/2019JB018053>
- Geist, D. J., Harpp, K. S., Naumann, T. R., Poland, M., Chadwick, W. W., Jr., Hall, M., & Rader, E. (2008). The 2005 eruption of Sierra Negra volcano, Galápagos, Ecuador. *Bulletin of Volcanology*, *70*(6), 655–673. <https://doi.org/10.1007/s00445-007-0160-3>
- Hefner, W., Nooner, S. L., Chadwick, W. W., Jr., & Bohnenstiehl, D. W. R. (2020). Revised magmatic source models for the 2015 eruption at Axial Seamount including estimates of fault-induced deformation. *Journal of Geophysical Research: Solid Earth*, *125*(4), e2020JB019356. <https://doi.org/10.1029/2020JB019356>
- Hefner, W. L., Nooner, S. L., Chadwick, W. W., Jr., Caress, D. W., Paduan, J. B., Bohnenstiehl, D. R., & Clague, D. A. (2021). Deformation models for the 2015-eruption and post-eruption inflation at Axial Seamount from repeat AUV bathymetry. In *Abstract V45B-0138 presented at 2021 Fall Meeting, AGU, New Orleans, LA, 13–17 December*.
- Hickey, B. M. (1979). The California current system—Hypotheses and facts. *Progress in Oceanography*, *8*, 191–279. [https://doi.org/10.1016/0079-6611\(79\)90002-8](https://doi.org/10.1016/0079-6611(79)90002-8)
- Hickey, B. M. (1989). Patterns and processes of shelf and slope circulation. In M. R. Landry, & B. M. Hickey (Eds.), *Coastal oceanography of Washington and Oregon* (pp. 41–115). Elsevier Science. [https://doi.org/10.1016/s0422-9894\(08\)70346-5](https://doi.org/10.1016/s0422-9894(08)70346-5)
- Inazu, D., Hino, R., & Fujimoto, H. (2012). A global barotropic ocean model driven by synoptic atmospheric disturbances for detecting seafloor vertical displacements from in situ ocean bottom pressure measurements. *Marine Geophysical Researches*, *33*, 127–148. <https://doi.org/10.1007/s11001-012-9151-7>
- Jónsson, S. (2009). Stress interaction between magma accumulation and trapdoor faulting on Sierra Negra volcano, Galápagos. *Tectonophysics*, *471*(1–2), 36–44. <https://doi.org/10.1016/j.tecto.2008.08.005>
- Kelley, D. S., Delaney, J. R., & Juniper, S. K. (2014). Establishing a new era of submarine volcanic observatories: Cabling Axial Seamount and the Endeavour Segment of the Juan de Fuca Ridge. *Marine Geology*, *352*, 426–450. <https://doi.org/10.1016/j.margeo.2014.03.010>
- Kilburn, C. (2012). Precursory deformation and fracture before brittle rock failure and potential application to volcanic unrest. *Journal of Geophysical Research*, *117*, B02211. <https://doi.org/10.1029/2011jb008703>

- Kilburn, C. R. J. (2018). Forecasting volcanic eruptions: Beyond the failure forecast method. *Frontiers of Earth Science*, 6, 133. <https://doi.org/10.3389/feart.2018.00133>
- Kilburn, C. R. J., De Natale, G., & Carlino, S. (2017). Progressive approach to eruption at Campi Flegrei caldera in southern Italy. *Nature Communications*, 8, 15312. <https://doi.org/10.1038/ncomms15312>
- Le Saout, M., Bohnenstiehl, D. R., Paduan, J. B., & Clague, D. A. (2020). Quantification of eruption dynamics on the north rift at Axial Seamount, Juan de Fuca Ridge. *Geochemistry, Geophysics, Geosystems*, 21, e2020GC009136. <https://doi.org/10.1029/2020GC009136>
- Levy, S., Bohnenstiehl, D. R., Sprinkle, P., Boettcher, M. S., Wilcock, W. S. D., Tolstoy, M., & Waldhauser, F. (2018). Mechanics of fault reactivation before, during, and after the 2015 eruption of Axial Seamount. *Geology*, 46, 447–450. <https://doi.org/10.1130/G39978.1>
- Lynn, R. J., & Simpson, J. J. (1987). The California Current system: The seasonal variability of its physical characteristics. *Journal of Geophysical Research: Oceans*, 92(C12), 12947–12966. <https://doi.org/10.1029/JC092iC12p12947>
- Manalang, D., Wilcock, W. S. D., Cram, G., Tilley, J., Harrington, M., & Martin, D. (2019). Testing the A-0-A approach to pressure gauge calibrations on cabled observatories. In *Abstract S33D-0616 presented at 2019 Fall Meeting, AGU, San Francisco, CA, 9–13 December*.
- Muramoto, T., Ito, Y., Inazu, D., Wallace, L. M., Hino, R., Suzuki, S., et al. (2019). Seafloor crustal deformation on ocean bottom pressure records with non tidal variability corrections: Application to Hikurangi margin, New Zealand. *Geophysical Research Letters*, 46(1), 303–310. <https://doi.org/10.1029/2018GL080830>
- Natalie, J., Soule, D. C., Crone, T. J., Chadwick, W. W., Jr., & Wilcock, W. S. D. (2018). The relationship between post-2015 eruption deformation and seismicity rates since the 2015 eruption at Axial Seamount using OOI data. In *Abstract V43G-0211 presented at 2018 Fall Meeting, AGU, Washington, DC, 10–14 December*.
- Nooner, S. L., & Chadwick, W. W., Jr. (2009). Volcanic inflation measured in the caldera of Axial Seamount: Implications for magma supply and future eruptions. *Geochemistry, Geophysics, Geosystems*, 10(2). <https://doi.org/10.1029/2008GC002315>
- Nooner, S. L., & Chadwick, W. W., Jr. (2016). Inflation-predictable behavior and co-eruption deformation at Axial Seamount. *Science*, 354(6318), 1399–1403. <https://doi.org/10.1126/science.aah4666>
- Nooner, S. L., Chadwick, W. W., Jr., Caress, D. W., Paduan, J. B., & Clague, D. A. (2017). Using high-resolution repeat AUV bathymetry to constrain magma dynamics at Axial Seamount. In *Abstract presented at IAVCEI 2017 General Assembly, 14–18 August, Portland, Oregon, USA*.
- Pawlowicz, R., Beardsley, B., & Lentz, S. (2002). Classical tidal harmonic analysis including error estimates in MATLAB using T_TIDE. *Computers & Geosciences*, 28, 929–937. [https://doi.org/10.1016/S0098-3004\(02\)00013-4](https://doi.org/10.1016/S0098-3004(02)00013-4)
- Peltier, A., Bachèlery, P., & Staudacher, T. (2009). Magma transfer and storage at Piton de La Fournaise (La Réunion Island) between 1972 and 2007: A review of geophysical and geochemical data. *Journal of Volcanology and Geothermal Research*, 184(1–2), 93–108. <https://doi.org/10.1016/j.jvolgeores.2008.12.008>
- Peltier, A., Famin, V., Bachèlery, P., Cayol, V., Fukushima, Y., & Staudacher, T. (2008). Cyclic magma storages and transfers at Piton de La Fournaise volcano (La Réunion hotspot) inferred from deformation and geochemical data. *Earth and Planetary Science Letters*, 270(3–4), 180–188. <https://doi.org/10.1016/j.epsl.2008.02.042>
- Poland, M., Miklius, A., Sutton, A. J., & Thornber, C. R. (2012). A mantle-driven surge in magma supply to Kilauea Volcano during 2003–2007. *Nature Geoscience*, 5, 295–300. <https://doi.org/10.1038/ngeo1426>
- Polster, A., Fabian, M., & Villinger, H. (2009). Effective resolution and drift of Paroscientific pressure sensors derived from long-term seafloor measurements. *Geochemistry, Geophysics, Geosystems*, 10(8). <https://doi.org/10.1029/2009GC002532>
- Robertson, R. M., & Kilburn, C. R. J. (2016). Deformation regime and long-term precursors to eruption at large calderas: Rabaul, Papua New Guinea. *Earth and Planetary Science Letters*, 438, 86–94. <https://doi.org/10.1016/j.epsl.2016.01.003>
- Roche, O., Druitt, T. H., & Merle, O. (2000). Experimental study of caldera formation. *Journal of Geophysical Research*, 105(B1), 395–416. <https://doi.org/10.1029/1999jb900298>
- Sasagawa, G. S., Cook, M. J., & Zumberge, M. A. (2016). Drift-corrected seafloor pressure observations of vertical deformation at Axial Seamount 2013–2014. *Earth and Space Science*, 3, 381–385. <https://doi.org/10.1002/2016EA000190>
- Sasagawa, G. S., & Zumberge, M. A. (2021). Drift corrected pressure time series at Axial Seamount, July 2018 to November 2021 – A progress report. In *Abstract G25A-0340 presented at 2021 Fall Meeting, AGU, New Orleans, LA, 13–17 December*.
- Sawyer, A. M. (2020). *Short-term fluctuations in magma supply at Axial Seamount, Juan de Fuca Ridge* (Masters Thesis, p. 76). University of North Carolina at Wilmington.
- Sawyer, A. M., Nooner, S. L., Chadwick, W. W., Jr., & Lau, T.-K. (2019). Short-term fluctuations in magma supply rate and magma dynamics at Axial Seamount. In *Abstract O51B-1487 presented at 2019 Fall Meeting, AGU, San Francisco, CA, 9–13 December*.
- Sohn, R. A., Barclay, A. H., & Webb, S. C. (2004). Microearthquake patterns following the 1998 eruption of Axial Volcano, Juan de Fuca Ridge: Mechanical relaxation and thermal strain. *Journal of Geophysical Research*, 109(B1), B01101. <https://doi.org/10.1029/2003jb002499>
- Sohn, R. A., Webb, S. C., & Crawford, W. C. (1999). Local seismicity following the 1998 eruption of Axial Volcano. *Geophysical Research Letters*, 26(23), 3433–3436. <https://doi.org/10.1029/1999gl900505>
- Tan, Y. J., Waldhauser, F., Tolstoy, M., & Wilcock, W. S. D. (2019). Axial Seamount: Periodic tidal loading reveals stress dependence of the earthquake size distribution (b value). *Earth and Planetary Science Letters*, 512, 39–45. <https://doi.org/10.1016/j.epsl.2019.01.047>
- Thomson, R. E., & Fine, I. V. (2021). Revisiting the ocean's nonisostatic response to 5-day atmospheric loading: New results based on global bottom pressure records and numerical modeling. *Journal of Physical Oceanography*, 51, 2845–2859. <https://doi.org/10.1175/JPO-D-21-0025.1>
- Thomson, R. E., Roth, S. E., & Dymond, J. (1990). Near-inertial motions over a mid-ocean ridge: Effects of topography and hydrothermal plumes. *Journal of Geophysical Research*, 95(C5), 7261–7278. <https://doi.org/10.1029/jc095ic05p07261>
- Vasconez, F., Ramón, P., Hernandez, S., Hidalgo, S., Bernard, B., Ruiz, M., et al. (2018). The different characteristics of the recent eruptions of Fernandina and Sierra Negra volcanoes (Galápagos, Ecuador). *Volcanica*, 1(2), 127–133. <https://doi.org/10.30909/vol.01.02.127133>
- Voight, B. (1988). A method for prediction of volcanic eruptions. *Nature*, 332(6160), 125–130. <https://doi.org/10.1038/332125a0>
- Waldhauser, F., Wilcock, W. S. D., Tolstoy, M., Baillard, C., Tan, Y. J., & Schaff, D. P. (2020). Precision seismic monitoring and analysis at Axial Seamount using a real-time double-difference system. *Journal of Geophysical Research: Solid Earth*, 125, e2019JB018796. <https://doi.org/10.1029/2019JB018796>
- Wallace, L. M., Webb, S. C., Ito, Y., Mochizuki, K., Hino, R., Henrys, S., et al. (2016). Slow slip near the trench at the Hikurangi subduction zone, New Zealand. *Science*, 352(6286), 701–704. <https://doi.org/10.1126/science.aaf2349>
- West, M. E., Menke, W., Tolstoy, M., Webb, S., & Sohn, R. (2001). Magma storage beneath Axial Volcano on the Juan de Fuca mid-ocean ridge. *Nature*, 413, 833–836. <https://doi.org/10.1038/35101581>
- Wilcock, W. S. D., Dziak, R. P., Tolstoy, M., Chadwick, W. W., Jr., Nooner, S. L., Bohnenstiehl, D. R., et al. (2018). The recent volcanic history of Axial Seamount: Geophysical insights into past eruption dynamics with an eye toward enhanced observations of future eruptions. *Oceanography*, 31(1), 114–123. <https://doi.org/10.5670/oceanog.2018.117>

- Wilcock, W. S. D., Manalang, D. A., Fredrickson, E. K., Harrington, M. J., Cram, G., Tilley, J., et al. (2021). A thirty-month seafloor test of the A-0-A method for calibrating pressure gauges. *Frontiers of Earth Science*, 8, 600671. <https://doi.org/10.3389/feart.2020.600671>
- Wilcock, W. S. D., Tolstoy, M., Waldhauser, F., Garcia, C., Tan, Y. J., Bohnenstiehl, D. R., et al. (2016). Seismic constraints on caldera dynamics from the 2015 Axial Seamount eruption. *Science*, 354(6318), 1395–1399. <https://doi.org/10.1126/science.aah5563>
- Wilcock, W. S. D., Waldhauser, F., & Tolstoy, M. (2017). *Catalog of earthquake recorded on Axial Seamount from January, 2015 through November, 2015 (investigators William Wilcock, Maya Tolstoy, Felix Waldhauser)*. Interdisciplinary Earth Data Alliance. <https://doi.org/10.1594/IEDA/323843>
- Xu, G., Chadwick, W. W., Jr., Wilcock, W. S. D., Bemis, K. G., & Delaney, J. R. (2018). Observation and modeling of hydrothermal response to the 2015 eruption at Axial Seamount, Northeast Pacific. *Geochemistry, Geophysics, Geosystems*, 19, 2780–2797. <https://doi.org/10.1029/2018GC007607>
- Yang, X., Davis, P. M., & Dieterich, J. H. (1988). Deformation from inflation of a dipping finite prolate spheroid in an elastic half-space as a model of volcanic stressing. *Journal of Geophysical Research*, 93, 4249–4257. <https://doi.org/10.1029/jb093ib05p04249>
- Yun, S.-H., Segall, P., & Zebker, H. A. (2006). Constraints on magma chamber geometry at Sierra Negra Volcano, Galápagos Islands, based on InSAR observations. *Journal of Volcanology and Geothermal Research*, 150, 232–243. <https://doi.org/10.1016/j.jvolgeores.2005.07.009>
- Yun, S.-H., Zebker, H. A., Segall, P., Hooper, A., & Poland, M. (2007). Interferogram formation in the presence of complex and large deformation. *Geophysical Research Letters*, 34, L12305. <https://doi.org/10.1029/2007gl029745>